Relating extratropical atmospheric heat transport to cyclone life cycle characteristics and numbers in Southern Hemispheric winter

Jan Zibell[1], Alejandro Hermoso[2], Aaron Donohoe[3,4], and Sebastian Schemm[1,5]

[1]Institute for Atmospheric and Climate Science, ETH Zurich, Zurich, Switzerland
[2]Climate and Environmental Physics and Oeschger Centre for Climate Change Research, University of Bern, Bern, Switzerland
[3]Department of Atmospheric Sciences, University of Washington, Seattle, WA, US
[4]Applied Physics Laboratory, University of Washington, Seattle, WA, USA
[5]Department of Applied Mathematics and Theoretical Physics, Centre for Mathematical Sciences, University of Cambridge, Cambridge, UK

Correspondence: Jan Zibell (jan.zibell@env.ethz.ch)

Abstract.

Outside the tropics, extratropical cyclones account for most of the poleward atmospheric heat transport, and extreme heat transport events are known to occur in their vicinity. Yet, it remains unclear how individual cyclones contribute to heat transport over the course of their lifetime and whether the seasonal heat transport — viewed from a zonally integrated standpoint — is determined by their number. This study adopts a cyclone-centered perspective to quantify in detail the relationship between poleward heat transport and the life cycle characteristics of extratropical cyclones in Southern Hemispheric winter. Specifically, objectively identified surface cyclone tracks derived from ERA5 data (1981–2021) are combined with a moist static energy (MSE) framework involving an eddy-mean decomposition of the heat transport.

It is found that the local transient eddy MSE flux maximizes during the cyclone intensification phase and is largest in the warm sector with a secondary maximum in the cold sector. A considerable fraction of the flux in the warm-sector is located well equatorward of the cyclone and thus outside the cyclonic region identified by the tracking algorithm. This leads to a latitudinal shift between maxima in cyclone frequency and transient eddy MSE fluxes. To bridge the gap between zonally integrated heat transport and contributions from individual cyclones, local vertically integrated transient eddy MSE flux events are attributed to cyclones based on spatial overlap with the identified cyclone area. Accumulated over their entire lifetime, the cyclones that become most intense generally are the ones that exhibit the largest zonally integrated cyclone-attributed heat transport. Despite a disproportionate contribution of the most intense cyclones to the cyclone-attributed transient eddy MSE fluxes, the relationship between the seasonal number of intense cyclones and the seasonal mean poleward transient eddy MSE flux is sensitive to details of the eddy-mean decomposition. This result indicates that low wavenumber background flows mask the influence of cyclone characteristics in the vertical, zonal, and seasonal integral. Notably, at 50° S the relationship between the overall cyclone number and total heat transport shows a peak. Further research on the interplay between synoptic and planetary MSE fluxes in the vicinity of cyclones is needed to understand to which extent the cyclone number may be constrained by the global energy imbalance.

1 Introduction

It is well known that extratropical cyclones intensify in regions of large baroclinicity, i.e., where horizontal temperature gradients are large and static stability is relatively low (e.g. Eady, 1949) — for instance near a land-sea contrast, sea ice edge, or the Gulf Stream sector. In addition, individual storms can be strengthened by the release of latent heat during condensation (e.g. Booth et al., 2013; Büeler and Pfahl, 2017), which takes place in the ascent regions along the fronts or within the cyclone center (e.g., Attinger et al., 2019; Rüdisühli et al., 2020). The growth of an individual extratropical cyclone can therefore be understood as baroclinic growth modulated by diabatic heat release and an associated poleward heat transport. The mean baroclinicity, which is a measure for the growth potential of extratropical cyclones (Lindzen and Farrell, 1980), thereby helps to explain why extratropical cyclones develop in localized geographic regions (called storm tracks). However, while it helps to explain the growth rates of cyclones, it does not explain the exact number of storms in a season or how changes in cyclone number and intensity relate to each other. A small number of intense cyclones, for example, may erode as much baroclinicity as many weak cyclones (Sinclair and Catto, 2022).

Within the warm sectors of cyclones, not only sensible heat is transported poleward but also the fraction of latent heat that is not immediately condensed. Thereby, cyclones account for the dominant fraction of the poleward latent heat fluxes throughout the Southern Hemispheric (SH) extratropics (Sinclair and Dacre, 2019) and into Antarctica (Tsukernik and Lynch, 2013). This poleward latent heat fluxes make a vital contribution to the global meridional atmospheric heat transport, which counteracts the radiative imbalance between the equator and the pole (Peixoto and Oort, 1992). Atmospheric heat transport is conveniently described by the flux of moist static energy (MSE). Traditionally, the MSE framework is a zonal mean framework. MSE is the sum of latent and dry heat and potential energy. MSE flux occurs on different time-scales and length-scales such that total heat transport is commonly decomposed into eddy and background flux contributions (e.g., Priestley, 1949; Barpanda and Shaw, 2017). The mean flow corresponds to the overturning circulation, which in the midlatitudes is the Ferrell cell that transports heat equatorward. Furthermore, low-frequency planetary-scale waves are associated with considerable poleward MSE flux especially in the Northern Hemisphere (NH, Barpanda and Shaw, 2017; Stoll et al., 2023). The largest share of midlatitude MSE flux is, however, related to transient synoptic-scale eddies (e.g. Peixoto and Oort, 1992; Armour et al., 2019; Stoll et al., 2023). In these frameworks, storm track activity is typically assessed in the zonal integral by defining the storm track latitude as the maximum in transient eddy MSE flux (Barpanda and Shaw, 2017; Shaw et al., 2018). This framework allows changes in the storm track latitude and intensity to be decomposed into changes in the hemispheric scale heat budget, i.e., the background heat transport, the heat storage, and energy input by radiative and turbulent fluxes. On the seasonal scale, for instance, the storm track response to radiative forcing in the NH is delayed by the stationary background circulation (Barpanda and Shaw, 2017). Alternatively, the zonally integrated heat transport can also be decomposed into contributions by different wavenumbers, which have been linked to the occurrence of weather regimes (Lembo et al., 2022). Although these existing approaches connect the zonally integrated atmospheric heat transport to local weather phenomena, the contributions of cyclones to the zonally integrated heat transport have not been systematically quantified.

Local (extreme) transient MSE fluxes have been linked to the warm- and cold-sectors of midlatitude cyclones (Messori and Czaja, 2015; Messori et al., 2017). These MSE flux peaks typically form banded structures which, in some cases, follow the frontal zones near surface cyclones (Geen et al., 2016; Messori et al., 2017). These events majorly contribute to the zonally integrated transient MSE flux (Messori and Czaja, 2013). In addition, days with enhanced zonally integrated transient MSE fluxes have a disproportionate impact on the seasonal integral (Messori and Czaja, 2015) suggesting that local extreme events may significantly contribute to climatological zonally integrated flux. On the other hand, it was found that local flux extremes arise from a combination of synoptic and planetary signals (Messori and Czaja, 2014). This indicates that transient MSE fluxes in the vicinity of a cyclone might not solely be determined by its life cycle characteristics but also contain contributions from low-frequency background flows. Despite these advances, a systematic analysis of when during the cyclone life cycle MSE fluxes maximize has not been performed. Consequently, it remains unclear which life cycle characteristic most strongly modulates the instantaneous zonally integrated transient MSE flux and how much individual cyclones contribute to the seasonally integrated flux (Messori and Czaja, 2015) depending on their characteristics.

This study is further motivated by the modeled decrease in cyclone numbers under global warming. Most studies that investigate cyclone numbers within coupled climate simulations agree that the cyclone number in SH winter decreases in a warmer climate (König et al., 1993; Geng and Sugi, 2003; Lambert and Fyfe, 2006; Grieger et al., 2014; Chang, 2017; Priestley and Catto, 2022) whereas Chang et al. (2012) identified no robust decrease apart from the Atlantic sector. This response to warming is also underpinned by highly idealized atmosphere-only experiments (Sinclair et al., 2020; Schemm et al., 2022). A plausible explanation for this reduction could be that, as individual cyclones transport more latent heat because of the Clausius-Clapeyron relationship (Geen et al., 2016), fewer cyclones account for same heat transport as in a present-day climate (Zhang and Wang, 1997). Yet, the total heat transport does not remain constant (as had been suggested by Boer, 1995) but exhibits a latitude-dependent response (Donohoe et al., 2020). Moreover, the change in MSE transported by individual cyclones likely also depends on the cyclone characteristics such as the intensity or spatial extent, which are projected to change as well (Dai and Nie, 2022; Priestley and Catto, 2022). Thus, how the partitioning of the total heat transport onto extratropical cyclones changes under warming is non-trivial. Addressing the storm track response to climate forcing therefore necessitates a more profound understanding of the relationship between zonally integrated heat transport and cyclone number and intensity under present climate conditions.

In this study, we aim to bridge the gap between the synoptic-scale cyclone and zonally integrated heat transport perspectives by investigating 41 years of reanalysis data. We make the assumption that the MSE flux related to cyclones is described by the transient eddy component of a flux decomposition, and hereafter refer to this simply as the transient MSE flux. Firstly, the spatio-temporal relationship between meridional transient MSE fluxes and extratropical cyclones is explored. Building on that, we inspect the contribution of a cyclone to the zonally integrated, meridional transient MSE flux — in other words its energy transport footprint — by introducing a feature-based approach to attribute transient MSE fluxes to individual cyclones. While trends in heat transport (and its sub-components) have been investigated in previous studies (Rydsaa et al., 2021; Clark et al., 2022; Simmons, 2022; Franzke and Harnik, 2023; Cox et al., 2024a; Kang et al., 2024), we examine the inter-annual variability of the seasonal cyclone number along with seasonal transient MSE fluxes. We focus on the SH storm track during

the winter months June, July, and August (JJA). In contrast to the NH, the SH storm track is nearly circumpolar and therefore more zonally symmetric, which simplifies linking zonally integrated fluxes to cyclone characteristics. Moreover, winter is the season during which cyclone activity is maximum. The specific research questions thus are:

- How does the local transient MSE flux evolve during the life cycle of extratropical cyclones?
- How much of the zonally integrated heat transport can be attributed to cyclones, and how do their contributions differ according to their key life cycle characteristics such as intensification rate, intensity, and lifetime?
- On a seasonal scale, how is the number of cyclones related to transient MSE flux, and more generally the total atmospheric heat transport?

The aim behind the last of the above research questions is to *diagnose* the existence of a relationship between atmospheric heat transport and the cyclone number. The methods applied in this study are detailed in Sect. 2. The evolution of transient MSE fluxes along cyclone life cycles, including spatial composites, is presented in Sect. 3. How cyclone characteristics influence the energy transport footprint of a cyclone in the zonal integral is shown and discussed in Sect. 4. The seasonal relationship between (transient) heat transport and extratropical cyclone number is examined in Sect. 5. Finally, the results are summarized and discussed in a broader context in Sect. 6.

2 Methods

2.1 Reanalysis data

All computations of this study are based on the ERA5 reanalysis (Hersbach et al., 2020), using six-hourly data of the years 1981 to 2021 during the winter season (DJF, i.e., December, January, February, in the NH and JJA in the SH). All variables are obtained at $0.5° \times 0.5°$ horizontal grid resolution.

2.2 Cyclone tracking

Automated cyclone tracking

Extratropical cyclones are identified using the cyclone tracking algorithm developed by Wernli and Schwierz (2006) and refined to improve the handling of splitting and merging events by Sprenger et al. (2017). Local minima of sea level pressure (SLP) are identified and followed over time. The cyclone mask is defined by the outermost closed SLP contour around a SLP minimum. Thereby, the outermost closed contour must be shorter than $7500\,\mathrm{km}$. The lifetime of a track is defined as the number of time steps of a track starting at genesis and including lysis. The maximum intensity is defined as the minimum SLP along a track and the growth rate as the change in SLP between two consecutive time steps. While cyclones are tracked using hourly SLP input, only six-hourly time steps are considered in the analysis to match the temporal resolution of the calculated MSE fluxes.

Track postprocessing

We focus on well-defined cyclone tracks with a clear growth phase in this study. Thus tracks are excluded tracks that are shorter than $24\,\mathrm{h}$ and with lowest central SLP above $990\,\mathrm{hPa}$ to remove spurious tracks in and around topography and thermal lows. Furthermore, we filter out tracks for which the maximum SLP reduction over $24\,\mathrm{h}$ normalized with $\frac{\sin 60°\mathrm{S}}{\sin \phi}$ is smaller than zero (Sanders and Gyakum, 1980). ϕ here represents the latitude of the cyclone center averaged over $24\,\mathrm{h}$. This alternative threshold for the intensification rate would also be referred to as $0\,\mathrm{Bergeron}$. As a reference, $1\,\mathrm{Bergeron}$ corresponds to a deepening rate of $24\,\mathrm{hPa\,d^{-1}}$ at $60°$ S. Lastly, we discard tracks that do not intensify poleward of $30°$ S, i.e., tropical cyclones without an extratropical transition.

Cyclone-centered composites

To investigate the transient MSE fluxes associated with cyclones, cyclone-centered composites are computed at different stages of the cyclone life cycle (e.g. time of maximum intensification). MSE fluxes are regridded such that the cyclone center is located at (0,0) in cyclone-centered coordinates. Bilinear interpolation is used for all fields except precipitation, where conservative remapping is employed. As we aim to investigate meridional fluxes, the resulting fields are *not* rotated along the direction of propagation to preserve the distinction between meridional and zonal winds and fluxes.

2.3 MSE fluxes

Zonal mean budget

To quantify atmospheric heat transport, we use the MSE framework. MSE is defined as $m = h + \Phi$ where the first contribution is the thermal energy of the atmosphere $h = c_p T + Lq$ where c_p is the specific heat capacity, L is the latent heat of evaporation, T is temperature, q denotes specific humidity, and Φ is geopotential. In the vertical integral and zonal average, the local atmospheric heat budget (as derived, for instance, in Trenberth, 1991) is written as

$$\partial_t \langle [h] \rangle = [F_{\mathrm{TOA}} - F_{\mathrm{S}}] - \partial_y \langle [vm] \rangle, \tag{1}$$

where F_{TOA} and F_{S} represent the net energy flux at the top of atmosphere (TOA) and surface, respectively, and v denotes meridional wind (Neelin and Held, 1987; Barpanda and Shaw, 2017). F_{TOA} is comprised of only radiative fluxes whereas F_{S} includes both radiative fluxes at the surface and turbulent fluxes. The temporal change in h is thus determined by the convergence of atmospheric heat flux and the net energy input at the surface and TOA.

The meridional divergence is computed as $\partial_y(\cdot) \equiv \partial_\phi\{\cos\phi(\cdot)\}/(a\cos\phi)$ and the vertical integral is mass-weighted ($\langle\cdot\rangle \equiv \frac{1}{g}\int_0^{\overline{p_{\mathrm{S}}}}(\cdot)dp$). The integral is computed from the TOA to the climatological mean surface pressure $\overline{p_{\mathrm{S}}}$ (Boer and Sargent, 1985). This formulation neglects kinetic energy and latent heat related to the liquid-ice transition (Mayer et al., 2024) and defines

fluxes relative to a fixed mass of atmosphere following Cox et al. (2024b). MSE fluxes are computed at 28 of the 37 available pressure levels spanning 1–1000 hPa[1].

Eddy-mean decomposition

We further decompose the MSE flux into eddy and mean components. Transient eddies are defined as deviations from a background mean state and are traditionally thought to be related to synoptic weather systems (e.g. Kaspi and Schneider, 2013; Barpanda and Shaw, 2017). One established approach defines the background state using monthly means, such that the monthly mean flux reads

$$[\overline{vm}] = [\overline{v'm'}] + [\overline{v}^*\overline{m}^*] + [\overline{v}][\overline{m}] \tag{2}$$

with dashes and asterisks signifying anomalies from the monthly $\bar{\cdot}$ and zonal averages $[\cdot]$, respectively (Priestley, 1949; Peixoto and Oort, 1992). Following Barpanda and Shaw (2017), the first two terms on the right hand side represent fluxes by transient and (temporally) stationary eddies, respectively, whereas the third term corresponds to the meridional overturning circulation.

To investigate the total MSE flux, we perform a correction to account for mass conservation which is not guaranteed in ERA5 (e.g., Mayer et al., 2021). In the zonal mean, mass-conservation corresponds to $\langle [v] \rangle = 0$ when calculating heat transport with respect to a time-independent atmospheric mass. We thus adopt the approach introduced by Marshall et al. (2014) and subtract vertical averages of $[m]$ and $[v]$ before computing the overturning circulation. Thereby, the MSE flux that is related to a net mass flux, which can be unrealistically large (Cox et al., 2023), is removed.

Sensitivity regarding the decomposition

Defining transient eddies as deviations from monthly mean data introduces discontinuities at the end of each month. We explore the sensitivities of the results using two additional definitions of transient eddies: (i) high-pass filtering (e.g. Hoskins et al., 1983; Schemm and Rivière, 2019; Franzke and Harnik, 2023) with a cut-off frequency of 10 d and; (ii) defining eddies as anomalies from instantaneous zonal means (Cox et al., 2024b). This eddy flux thus depends on the atmospheric state up- and downstream at the same latitude. In contrast, the eddy flux in the other two methods depends on the characteristics of the time series of the data at the same location.

Throughout the manuscript, we use superscripts to indicate anomalies: A prime $(\cdot)'$ for deviations from a temporal mean (referred to as 'transient' anomaly), and $(\cdot)^*$ for deviations from the zonal mean. A corresponding subscript indicates the method used for the computation of the background state. A subscript MA indicates monthly anomalies, HP refers to high-pass filtering, and ZA indicates zonal anomalies. Thus, in sensitivity tests we compare $v'm'_{\mathrm{MA}}$ to $v'm'_{\mathrm{HP}}$ and $v^*m^*_{\mathrm{ZA}}$. A complete list of the used mathematical symbols is provided in Appendix A.

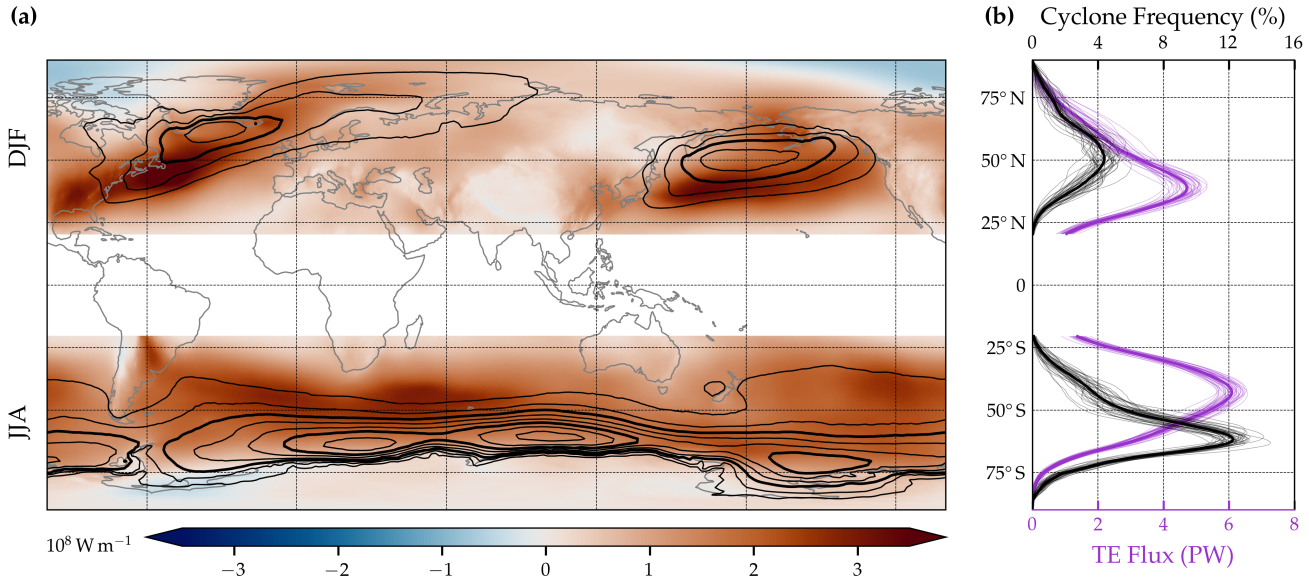

Figure 1. Climatologies of transient MSE fluxes and cyclone frequencies during winter for both hemispheres (DJF in the NH and JJA in the SH.) **(a)** Vertically integrated and seasonally averaged transient MSE fluxes, $\langle \overline{v'm'}_{\mathrm{MA}} \rangle$, (shading) are shown along with the cyclone mask frequency (black contours in steps of 5 % starting at 5 % with 15 % and 30 % highlighted in thicker contours). **(b)** Zonally integrated transient MSE fluxes, $\langle [\overline{v'm'}_{\mathrm{MA}}] \rangle$, (purple) and zonal mean cyclone frequencies (black) for individual seasons (thin lines) and the climatology thereof (solid lines). MSE fluxes are shown positive poleward. Note that the cyclone frequency in **(b)** is multiplied with the cosine of latitude for consistency.

2.4 Cyclone-attributed MSE fluxes

In this section it is described how local MSE fluxes are attributed to individual cyclones. Having computed cyclone masks from the SLP fields, the simplest approach is to spatially integrate the MSE fluxes over the cyclone mask at each timestep. Note, however, that climatologically the maximum transient MSE flux is located equatorward of the maximum in surface cyclone frequencies (Fig. 1a). This is similar to the relationship between surface cyclones and eddy kinetic energy (e.g., Shaw et al., 2016). Schemm et al. (2018) argue that this latitudinal offset occurs because eddy fluxes peak during the rapid growth phase of extratropical cyclones, whereas cyclone detection frequencies peak in regions where cyclones have evolved into mature, slowly propagating systems. This latitudinal offset is also evident in the zonal mean (Fig. 1b): In the SH, transient MSE flux peaks at 6 PW around 45° S, while the zonally integrated cyclone frequency reaches up to 12 % near 62° S. Thus, most of the transient MSE fluxes are expected to be excluded when spatially integrating fluxes only within the (SLP-based) cyclone masks.

[1]The exact levels used are 1, 3, 5, 10, 30, 50, 100, 150, 200, 250, 300, 350, 400, 450, 500, 550, 600, 650, 700, 750, 800, 850, 875, 900, 925, 950, 975, and 1000 hPa. Note that we ensured that the sub-selection of vertical levels has minimal impact on the monthly closure of the energy budget.

To overcome this latitudinal gap between the two storm track metrics, a flux attribution method is introduced that identifies coherent MSE flux features and connects them to cyclones via spatial overlap criteria. Transient MSE flux features in this work are identified using a percentile threshold (similarly to studies tracking atmospheric rivers, Shields et al., 2018). The flux threshold is chosen to be latitude- and time-dependent to account for the high spatial and temporal variability of MSE. The percentile is drawn from all values of a latitude band at the same time step of each year, (see Fig. B1). Thus, it is computed from 29,520 values ($360°/\text{gridspacing} \times$the number of years as illustrated in Fig. B2). Given a percentile rank p, the vertically integrated transient flux $\langle v' m'_{\text{MA}} \rangle$ is masked using the flux thresholds corresponding to $p > 0.5$ for northward fluxes and $1 - p$ for southward fluxes.

A well-defined MSE flux feature mask is defined by adjacent grid points at which the percentile threshold is exceeded. The features are identified and labeled using TempestExtremes v2.1 (Ullrich et al., 2021). Small features ($4.9 \times 10^4\,\text{km}^2$ or approximately $1° \times 1°$), which are located predominantly in the tropics and subtropics, are discarded. The remaining features (describing both poleward and equatorward flux) are attached to cyclone tracks if they spatially overlap with the SLP-based cyclone masks (filled orange and blue patches in Fig. 2). This is done at every timestep separately as the MSE flux features are not tracked (or "stitched" in the language of the tool) over time. Non-overlapping MSE features are labeled as 'other MSE fluxes' (orange and blue contours in Fig. 2). If a flux mask overlaps with multiple cyclones, the cyclone with the lowest center SLP is chosen. Randomly selecting between the overlapping cyclones was also tested, but had no qualitative effect on the results. Note that given the percentile rank p, the ratio of grid points attributed to cyclones is not exactly $2 \cdot (1 - p)$ ('northward' plus 'equatorward' areas) but less because of filtering out small features and not all of the remaining are attributed to cyclones. Due to the relative simplicity of the attribution method, sensitivity analyses boil down to the choice of p and the flux decomposition method. While the results in Sects. 4 and 5 are for $p = 0.9$, $p = 0.8$ and $p = 0.95$ were also tested. The percentile generally determines the width of the attributed features. The location of these features in turn differs depending on the decomposition method (Fig. B2).

From local fluxes to the zonal budget

In the zonal heat budget, the MSE flux attributed to a cyclone is simply the zonal integral of the flux within the attributed MSE flux features (orange curve in Fig. 2). To define the cyclone number at each latitude, each cyclone is counted once towards all latitude bands where its attributed MSE flux is different from zero along its lifetime (purple bars in Fig. 2). Thus, the seasonal number of cyclones at a given latitude corresponds to the cyclones that have attributed transient MSE flux at this latitude, whereas their corresponding life cycle characteristics, such as maximum intensification rate or maximum intensity, can occur at any latitude.

The seasonal sets of strongly intensifying cyclones are then determined using climatological thresholds: Cyclones are considered 'strongly' intensifying if their intensification rate lies above the 75$^{\text{th}}$ percentile determined from the climatological set of all cyclones passing that latitude. If the 75$^{\text{th}}$ percentile of cyclone intensification based on all SH JJA cyclones is, for instance, $24\,\text{hPa}\,\text{d}^{-1}$, then this threshold defines the number of strongly intensifying cyclones in every season. Thus, their number is *not* simply 25 % of the seasonal number if that year has more or less strongly intensifying storms than the climatology. Choos-

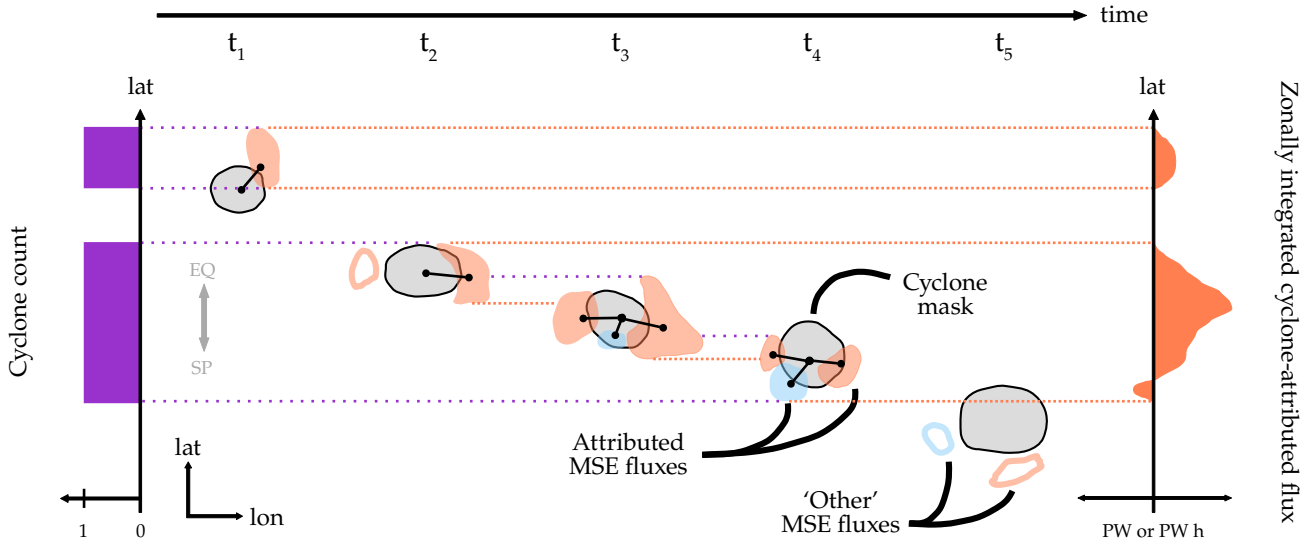

Figure 2. The attribution of transient MSE flux to surface cyclones exemplified for a cyclone that lasts for five six-hourly time steps. The cyclone mask is indicated with grey patches and the attributed poleward and equatorward transient MSE flux features with orange and blue shading, respectively. Other MSE fluxes that are not spatially overlapping are shown with orange and blue contours. In the zonal integral, cyclone-attributed transient MSE fluxes are expressed in PW h if accumulated or in PW if averaged over the cyclone lifetime (orange curve). The latitudinal extent used for counting is then determined by the latitudes at which the attributed fluxes along its lifetime are non-zero. At any latitude band, a cyclone is therefore counted either once or zero times (purple bars). A grey arrow serves orientational purposes.

ing the 75$^{\text{th}}$ percentile (instead of the 90$^{\text{th}}$, for instance) is found to be an adequate compromise between selecting only the strongest cyclones and including a large enough number of cyclones to counteract the event-to-event variability (see discussion in Appendix D). If the intensification rate lies within the inter-quartile range or below, cyclones are denoted 'moderately' or 'weakly' intensifying, respectively. The classification of cyclones as 'strong', 'moderate', and 'weak' works analogously for intensity.

These methods enable us to study the relationship between various extratropical cyclone life cycle characteristics and MSE fluxes. They also allow us to analyze the fractional contribution of cyclone-related MSE flux to the zonally integrated poleward heat transport and the relationship between cyclone number and intensity and zonally integrated atmospheric heat transport. By defining the number of cyclones as where they contribute to MSE flux we can study the linkage between cyclone numbers and heat transport in a consistent way.

3 Transient MSE fluxes along extratropical cyclones

First, it is investigated how the local transient MSE fluxes ($v'm'_{\text{MA}}$) evolve along the extratropical cyclone life cycle and where they maximize relative to the cyclone center.

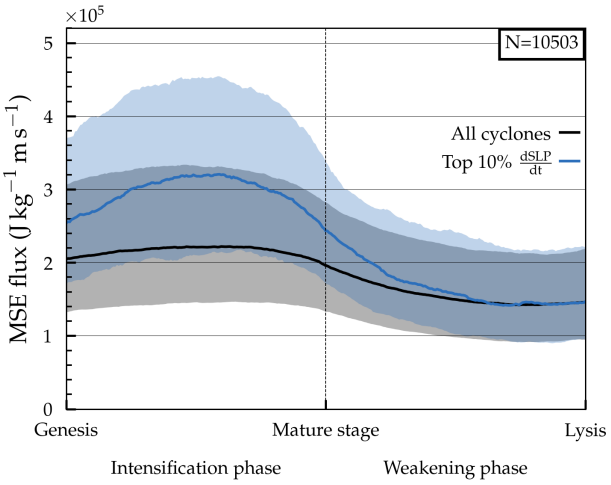

Figure 3. Maximum near-cyclone transient MSE flux, $v'm'_{\mathrm{MA}}$, at $850\,\mathrm{hPa}$ for all (black) and the $10\,\%$ most strongly intensifying cyclones (blue) along the normalized cyclone life cycle. The search radius is $7.5°$. Median and interquartile range are shown in solid lines and shading, respectively. Genesis and lysis correspond to the first and last time steps of the track, respectively, while the mature stage is defined as the time of minimum central SLP. The number of all SH cyclones is included in the upper right.

3.1 Temporal evolution of transient MSE flux during the life cycle of extratropical cyclones

To compare extratropical cyclones life cycles of different durations the transient MSE flux is interpolated to a normalized cyclone life cycle (e.g. Rudeva and Gulev, 2007; Schemm et al., 2018). Following previous studies, cyclone tracks are split into an intensification and a weakening phase and tracks with less than two time steps in each phase are removed from the analysis. The maximum transient MSE flux at $850\,\mathrm{hPa}$ within a $7.5°$ radius around the cyclone center is interpolated to the normalized life cycle using cubic spline interpolation (Fritsch and Carlson, 1980; Schemm et al., 2018).

Considering all SH cyclones, $v'm'_{\mathrm{MA}}$ peaks before mature stage and declines afterwards (black line in Fig. 3). The peak flux during intensification is, on average, around $50\,\%$ larger than during the weakening phase. This evolution is broadly consistent with the baroclinic life cycle, in which transient eddy heat flux peaks as baroclinicity is eroded, before intensification terminates (Novak et al., 2015). Using larger attribution radii does not qualitatively affect this result, but it increases the proportion of flux attributed to a cyclone that, upon visual inspection, would be attributed to a nearby cyclone. For the $10\,\%$ most strongly intensifying cyclones, the peak of MSE flux during genesis is exaggerated with a median flux of roughly $50\,\%$ larger during the intensification phase compared to all cyclones (blue line in Fig. 3). In turn, similar flux values are observed during the weakening phase. This highlights the close relationship between transient MSE flux and the intensity of baroclinic growth. The following spatial analyses will thus focus entirely on the intensification phase.

3.2 Spatial relation of transient MSE fluxes and cyclones

The spatial distribution of MSE fluxes around the cyclone center is studied using cyclone-centered composites. Recall that in the SH, cyclonic flow is *clockwise* and that *poleward* flux is chosen *positive*. Also, both the poleward transport of anomalously warm moist as well as the equatorward transport of anomalously cool and dry air result in a positive poleward MSE. Thus the warm and cold sectors both show up as positive MSE fluxes in the composites.

The composite based on all cyclones indicates a maximum in poleward $v'm'_{\mathrm{MA}}$ at the $850\,\mathrm{hPa}$ level in the warm sector of the cyclone center during all three key stages the cyclone life cycle (Fig. 4a–c). The MSE flux is generally larger on the equatorward side of the cyclone center. This is consistent with previous findings that heat transport is bound by the frontal zones (compare, for instance, with the $990\,\mathrm{hPa}$ lines in Fig. 4; Geen et al., 2016; Messori et al., 2017) which in the SH frequently extend to 20–40° S which is well equatorward of the cyclone centers (Schemm et al., 2015; Rudeva et al., 2019). Closer inspection of the peak at genesis indicates that, in some cases, the flux is associated with a cold front accompanying a mature cyclone further downstream. This suggests that some cases are secondary cyclogenesis events, when a cyclone growths on the pre-existing front of a mature system (Schemm and Sprenger, 2015). During mature stage, the location of the maximum poleward flux is located further downstream in the warm sector relative to its position at genesis, when it is located closer to the cold front. In addition, a negative flux upstream of the cyclone center emerges at $\mathrm{rlon} = -1^\circ$, $\mathrm{rlat}{=}0^\circ$ in the local coordinates (light blue patch in Fig. 4c).While the warm sector features a local flux peak during all life cycle stages, the cold sector displays a well-marked positive flux signal in the composites only at the mature stage (Fig. 4c).

In vertical west-to-east cross-sections through the cyclone center, the pronounced warm sector flux extends up to roughly $300\,\mathrm{hPa}$ during all stages and reaches its maximum at around $900\,\mathrm{hPa}$ (Fig. 4d–f). This signal is the footprint of the ascending warm and moist airstream known as warm conveyor belt, which was also identified by centering around 850 MSE flux extremes instead of cyclone centers (Messori and Czaja, 2015). The aforementioned negative flux located near the cyclone center extends up to around $700\,\mathrm{hPa}$, while around $500\,\mathrm{hPa}$ a second negative signal downstream of the center appears (Fig. 4f). All of the flux signals discussed here are significantly different from climatology (see Appendix C, Fig. C1).

To better understand the negative flux anomalies, consideration is given to composite mean meridional winds (grey lines in Fig. 4d–f). Overall, the wind anomalies tilt westward with height during intensification and become more barotropic at mature stage[2] which agrees with baroclinic theory (Eady, 1949; Thorncroft et al., 1993). For the mature stage, the wind field suggests that the mid-level negative flux signal at the $500\,\mathrm{hPa}$ level results from cold air moving poleward (Fig. 4f) and that the low-level equatorward flux represents warm and moist air flowing equatorward along the bent-back extension of the warm front (Shapiro and Keyser, 1990). The latter signal does not emerge when centering on flux extremes.

The composite analysis confirms the previous findings based on normalized tracks that meridional transient MSE fluxes near cyclones are, on average, largest during the intensification phase. Likewise, from a spatial composite perspective, the flux of the $10\,\%$ most strongly intensifying cyclones is roughly $50\,\%$ larger in the cold sector and up to $80\,\%$ larger in the warm sector compared to all cyclones (cf. Fig. 5a to Fig. 4b at $850\,\mathrm{hPa}$). Strongly intensifying cyclones feature negative fluxes at $300\,\mathrm{hPa}$

[2]While v' is shown in Fig. 4, this is also the case for the full meridional wind v (Fig. C1).

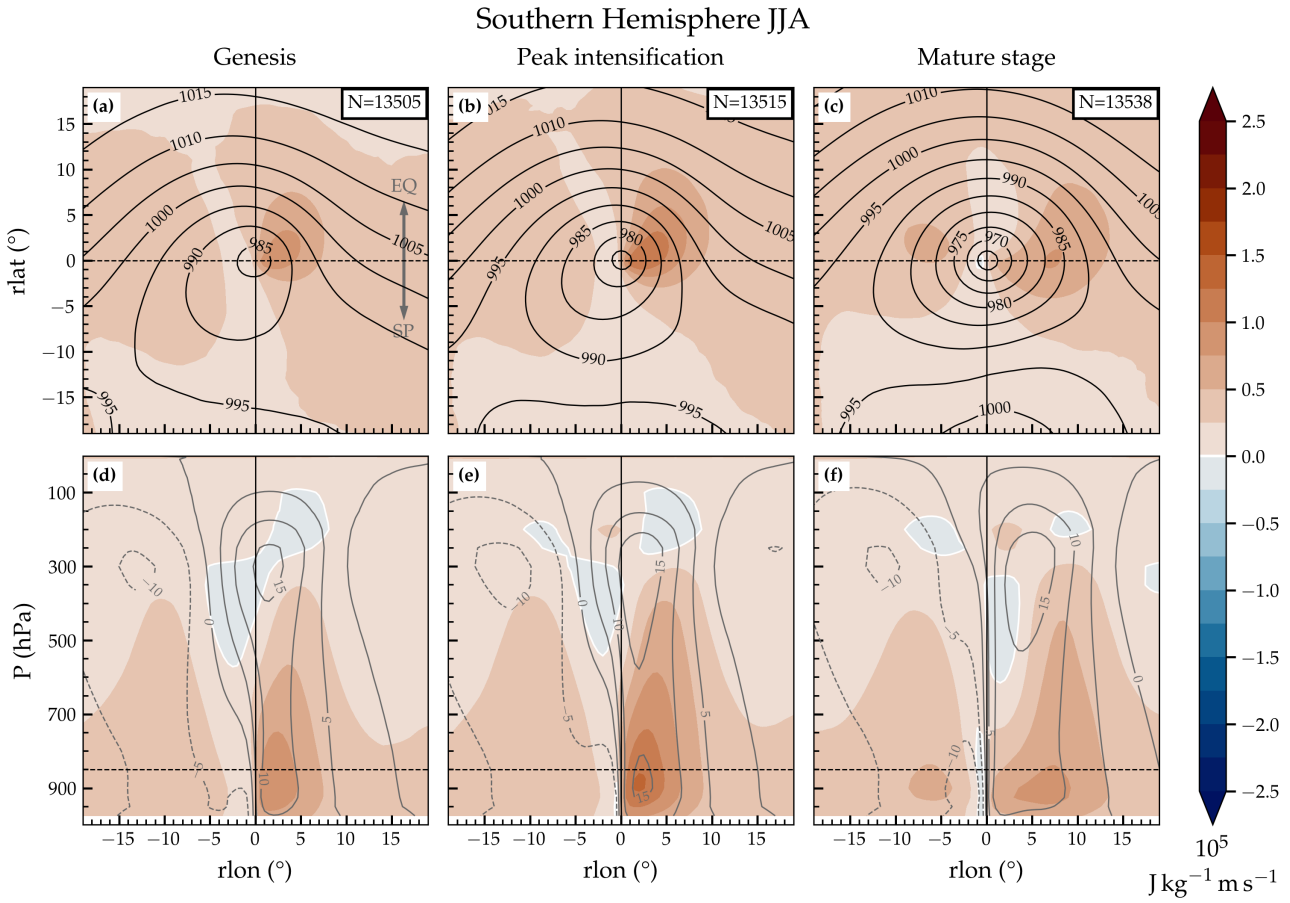

Figure 4. Cyclone-centered meridional transient MSE flux, $v'm'_{\mathrm{MA}}$, composited for different stages along the cyclone life cycle. Horizontal maps are shown for fluxes (colors) at 850 hPa for **(a)** genesis, **(b)** time of peak intensification, and **(c)** mature stage. Black contours indicate composite mean SLP in hPa. In panels **(d)–(f)**, the west-to-east cross-sections through $\mathrm{rlat} = 0$ correspond to the same stages as above. Grey lines depict meridional wind velocities (v') in $\mathrm{m\,s^{-1}}$ (positive poleward). Horizontal dashed black lines represent the intersection of the corresponding vertical and horizontal panels. Furthermore, the number of cyclones in the composites are included in the upper right in panels **(a)–(c)**. A grey arrow is included for better orientation indicating directions of equator (EQ) and South Pole (SP).

280 downstream of the center, which can be related to the anticyclonic return flow of the warm conveyor belt and which are less prominent in the composites of all SH cyclones (compare Fig. 5c and Fig. 4e).

These conclusions remain unchanged when cyclones with the deepest SLP values are considered instead of those that deepen most strongly. The corresponding warm and cold sector fluxes are more horizontally and vertically extended and the warm sector peak is slightly reduced (at peak intensification, Fig. 5b, d). This confirms the findings of earlier studies which argue
285 that, while very deep cyclones cover typically wider areas, they are not necessarily the cyclones that intensify most rapidly (Rudeva and Gulev, 2007).

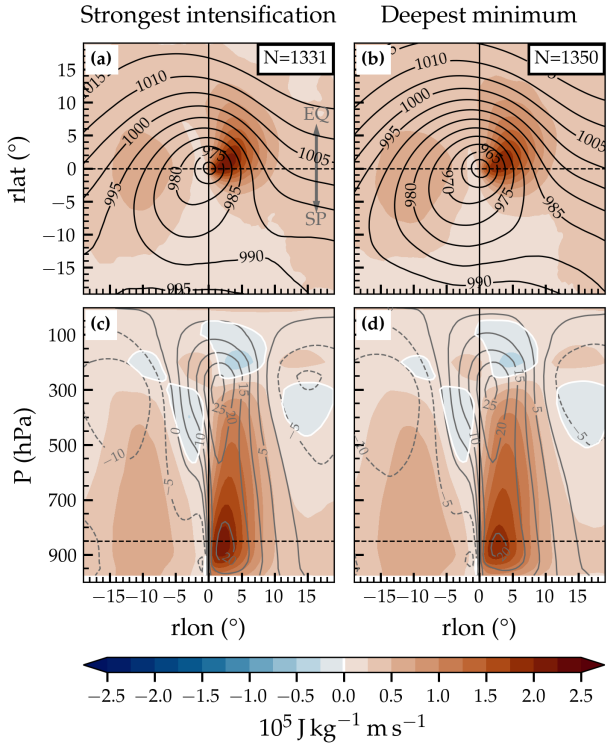

Figure 5. Cyclone-centered transient MSE flux at $850\,\mathrm{hPa}$ composited during time of peak intensification for **(a)** the $10\,\%$ most strongly intensifying cyclones and **(b)** the $10\,\%$ deepest cyclones at mature stage. Black contours indicate composite mean SLP in hPa. As in Fig. 4, panels **(c, d)** show the corresponding west-to-east cross-sections. Grey lines depict meridional wind velocities (v') in $\mathrm{m\,s^{-1}}$ (positive poleward). Horizontal dashed black lines represent the intersection of the corresponding vertical and horizontal panels. Furthermore, the numbers of cyclones in the composites are included in panels **(a, c)**. A grey arrow is included for better orientation indicating directions of equator (EQ) and South Pole (SP).

The asymmetry in the MSE flux between the cold and warm sectors is strongly related to the presence of moisture in the warm sector. However, MSE flux extremes can be related to both warm and cold sectors (Messori and Czaja, 2015) and in the seasonal mean, cold air advection contributes up to $40\,\%$ to the total poleward heat transport Messori et al. (2017). In the
290 composites, the warm sector flux stands out more strongly, which could be related to the fact that compositing by the cyclone center implies a tendency to centering next to the warm sector. Since the warm sector narrows during the life cycle as the cold front catches up with the warm front, the fluxes in the warm sector are spatially more constrained than in the broader cold sector (Shapiro and Keyser, 1990).

3.3 Latitudinal variations of dry and latent heat flux contribution to the MSE flux

The contribution of latent heat flux to the MSE flux varies with latitude, which results from the latitudinal distribution of specific humidity. To explore the dependency of the relative contributions by dry and latent energy on latitude, the top $10\,\%$ of cyclones with the strongest intensification are sorted into 10° latitude bands according to their centre latitude at peak intensification.

Both MSE and latent heat flux decrease for cyclones closer to the pole (Fig. 6). The maximum of $v'Lq'_{\mathrm{MA}}$, which is confined to the warm sector, largely overlaps with six-hourly accumulated precipitation (black contours in Fig. 6d,e). The relative contribution of $v'Lq'_{\mathrm{MA}}$ reduces for cyclones propagating closer to the pole as expected due to the Clausius-Clapeyron relationship (black contours in Fig. 6a–c). As a result, the contrast between fluxes in the warm and cold sectors almost vanishes for cyclones intensifying within 60–70° S (Fig. 6c). This explains the larger relative importance of cold air outbreaks to the heat budget towards higher latitudes (Messori et al., 2017).

Overall, the cyclone-centered perspective confirms and expands on previous findings on (low-level) transient eddy MSE flux extremes (Messori and Czaja, 2015; Geen et al., 2016; Messori et al., 2017). As the following sections discuss vertically integrated MSE fluxes, it is worth pointing out that the findings regarding the horizontal structure of transient MSE fluxes also apply to vertically integrated fluxes (and fluxes calculated using different decompositions, see Appendix C).

4 How do cyclone life cycle characteristics shape the zonally integrated heat flux?

The aim of this section is to understand the contributions of cyclones to the zonal integrated transient MSE flux, $\langle[v'm'_{\mathrm{MA}}]\rangle$ and to quantify to what extend their contributions differ depending on the specific life cycle characteristics such as intensification rate, maximum intensity, and lifetime. Messori and Czaja (2015) showed that zonally integrated MSE flux extremes are driven by coexisting warm and cold sectors and that a few zonal flux extremes have a disproportionate impact on the seasonal mean flux. A guiding question is thus: Do strongly intensifying cyclones shape the zonally integrated heat transport, or do the maximum intensity or lifetime matter more? To answer this question, we use the newly introduced MSE flux attribution method.

4.1 Contribution of cyclone-attributed MSE flux to the zonal budget

The zonal integral of the seasonal mean cyclone-attributed transient MSE flux, denoted as $\langle[\overline{v'm'}^{\mathrm{cycl}}_{\mathrm{MA}}]\rangle$, amounts to $1.65\,\mathrm{PW}$ at around 50° S (orange solid line in Fig. 7a)[3]. Thus, around $30\,\%$ of the overall transient MSE flux is attributed to cyclones (Fig. 7b), while the rest is attributed as non-cyclone related MSE flux. The correlation between the seasonal mean of the zonally integrated MSE flux and the cyclone-attributed transient MSE flux ranges from 0.5 around 40° S to 0.75 poleward of 55° S (orange line in Fig. 7c). Due to the presence of other dynamical features, for example anticyclones, and the degrees of freedom when attributing MSE flux to cyclone masks, which are discussed in Sect. 2.4, one must not expect $100\,\%$ flux coverage or perfect correlation.

[3]From this section onward, the overbar in $\langle[\overline{v'm'}^{\mathrm{cycl}}_{\mathrm{MA}}]\rangle$ denotes the *seasonal* mean.

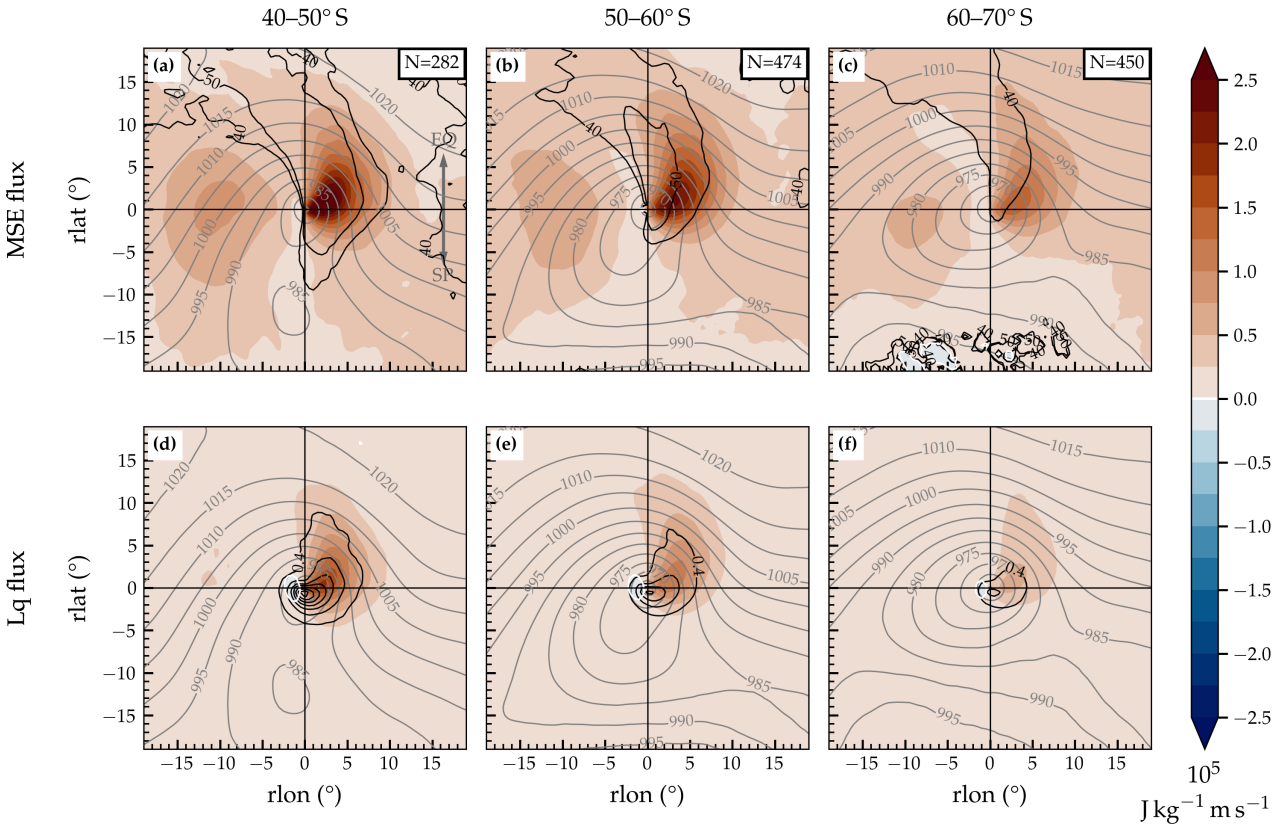

Figure 6. Cyclone-centered transient MSE flux, $v'm'_{\mathrm{MA}}$, at 850 hPa composited during time of peak intensification for cyclones with center within **(a)** 40–50° S, **(b)** 50–60° S, and **(c)** 60–70° S. Shading in **(d)–(f)** indicates the latent heat flux, $v'Lq'_{\mathrm{MA}}$. Regions where latent heat flux makes up for 40 % and 50 % of the MSE flux are outlined with black contours in **(a)–(c)**. Black lines in **(d)–(f)** depict precipitation in steps of $0.4\,\mathrm{mm\,h^{-1}}$. Grey contours indicate composite mean SLP in hPa. The number of cyclones in the composites are included in panels **(a)–(c)**. A grey arrow is included for better orientation indicating the directions of the equator (EQ) and South Pole (SP).

Note that the transient MSE flux located within the SLP-based cyclone masks is less than 1 PW (black dashed line in Fig. 7a). This low fraction (≈ 10 % at 50° S, Fig. 5b) is consistent with large fluxes occurring at the boundary and outside of the cyclone masks. Accordingly, a low to negative correlation is found between the seasonally averaged total and transient MSE fluxes within only the cyclone mask (black line in Fig. 7c). Based on the overlap method, we find the peak of the cyclone-attributed MSE fluxes at around 50° S, and therefore much closer to the MSE flux maximum near 42° S, while the fluxes within the SLP-based cyclone masks much further poleward (62° S). This is consistent with the fact that transient MSE flux peaks equatorward of the cyclone center along the trailing fronts. By bridging the latitudinal gap between the surface cyclone tracks and transient MSE fluxes (see also Fig. 1b), the overlap method is a comprehensive solution to connecting the two storm

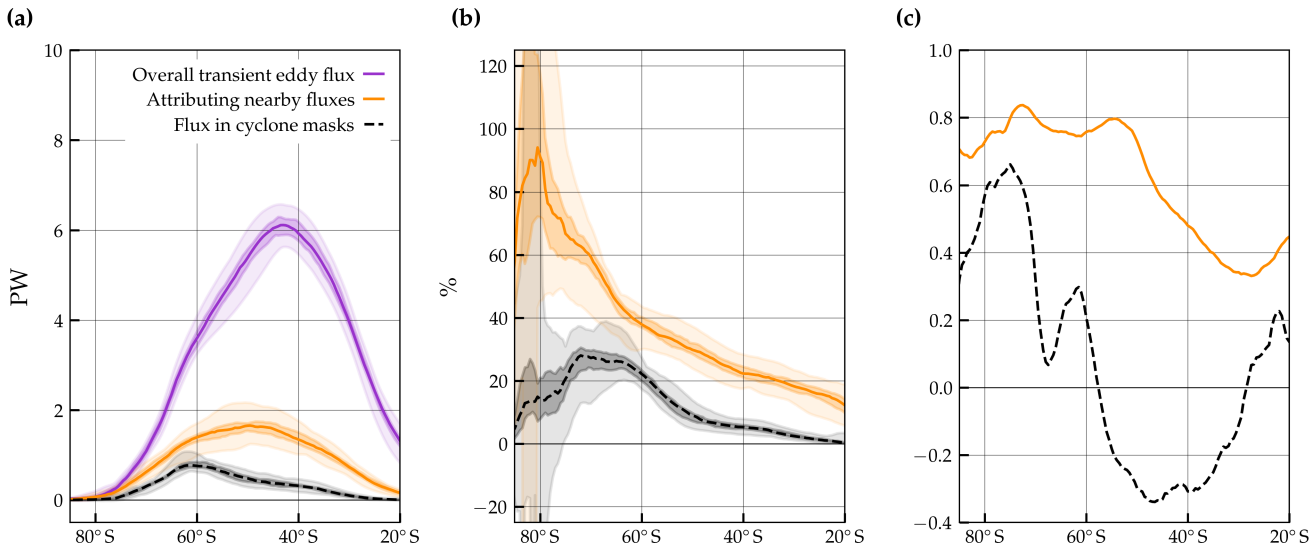

Figure 7. Seasonal transient MSE fluxes in SH winter: **(a)** the overall transient MSE fluxes, $\langle[\overline{v'm'}_{\mathrm{MA}}]\rangle$, shown in purple are contrasted to the transient MSE fluxes within features that are attributed to cyclones, $\langle[\overline{v'm'}^{\mathrm{cycl}}_{\mathrm{MA}}]\rangle$ (orange) and the transient MSE fluxes within cyclone masks (black, dashed). Solid and dashed lines indicate medians, light shading the full range, and darker shading the inter-quartile range of the seasonal means. **(b)** The percentage of the overall transient MSE flux attributed to cyclones (orange) and within the cyclone masks (black). **(c)** Correlations between seasonally averaged overall transient MSE fluxes and the fraction attributed to cyclones using the overlap method (orange) and with the SLP-based cyclone masks (black dashed).

track metrics. Qualitatively, the results are robust relative to the choice of the percentile and flux decomposition method (see Appendix D, Fig. D1).

4.2 Relevance of cyclone life cycle characteristics for the zonally integrated heat transport

Next, we address how life cycle characteristics influence the contribution of individual cyclones to the zonally integrated MSE flux. The contribution of a cyclone is defined as the attributed MSE flux along the track over the cyclone lifetime. We compare the accumulated MSE flux of 200 strongest and weakest cyclones (as done in Catto et al., 2010; Sinclair et al., 2020).

At $50°$ S, the lifetime-accumulated transient MSE flux of the 200 cyclones that intensify most strongly corresponds to $20\,\mathrm{PW\,h}$ (blue solid line in Fig. 8a). In turn, the 200 cyclones with the lowest intensification rates on average accumulate only a few $\mathrm{PW\,h}$, which peaks further poleward at around $65°$ S (red solid line in Fig. 8a). Thus, cyclones intensifying strongly accumulate 3–20 times the zonally integrated transient MSE flux of weakly intensifying cyclones (solid purple line in Fig. 8b).

The ratio found for strongest intensification is similar for the lifetime (dashed line in Fig. 8b). Cyclone intensity also emerges to be a clear differentiator for accumulated transport. The fluxes of the most intense cyclones are located further poleward

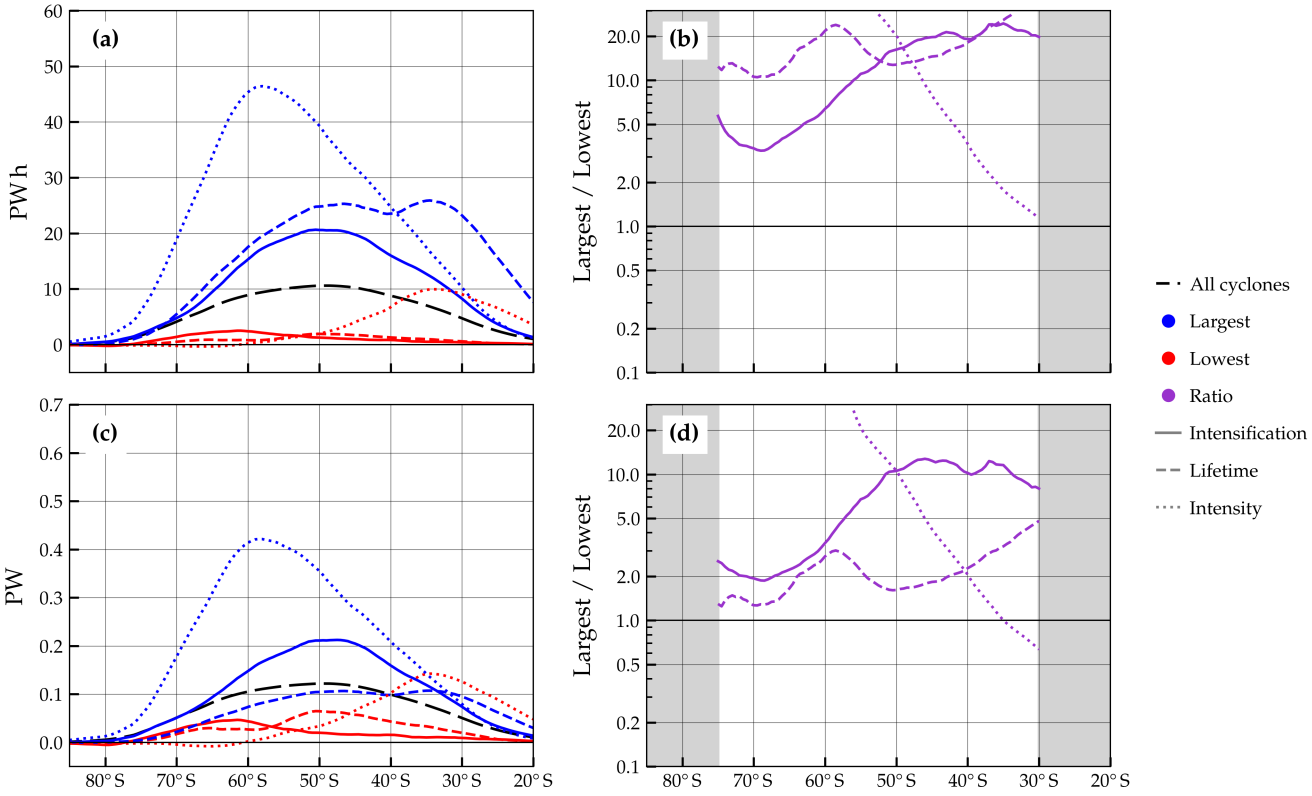

Figure 8. (a) Average zonally and vertically integrated transient MSE flux attributed to extratropical cyclones, $\langle [v'm'^{\,\mathrm{cycl}}_{\mathrm{MA}}] \rangle$, grouped by characteristic. Instantaneous vertically integrated fluxes are integrated temporally over the lifetime of each cyclone and integrated longitudinally at each latitude (unit PW h). For each characteristic, the flux of the 200 cyclones with the largest values of that characteristic is shown in blue and the lowest 200 ones in red, respectively. Solid, dashed, and dotted lines indicate intensification rate, lifetime, and intensity, respectively. For example, the most intense cyclones are shown by the blue dotted line. **(b)** Dividing the flux of the 200 largest cyclones by the flux of the 200 lowest cyclones yields the ratio for each characteristic with the same line-styles as in **(a)**. **(c, d)** As in **(a, b)**, respectively, but for the average flux per time step in PW. In panels **(a, c)**, the average fluxes computed from all SH JJA cyclones (from which the other subsets are chosen) are shown with black long dash lines. The ratio in panels **(b, d)** is masked out at latitudes where the absolute fluxes are close to zero.

compared to the weakest cyclones (dotted lines in Fig. 8a). This can be partly explained by SLP climatologically decreasing towards the pole. The corresponding ratio in Fig. 8b (dotted line) thus increases towards the pole.

To investigate whether strongly intensifying and intense cyclones only transport more heat because they possibly exist longer we also compare lifetime average MSE fluxes by normalizing accumulated fluxes by cyclone lifetime. Strongly intensifying cyclones are associated with a lifetime-averaged flux of 0.2 PW peaking near 50° S (solid lines in Fig. 8c), whereas the least intensifying cyclones transport roughly 10 times less at this latitude (Fig. 8d). In turn, the lifetime-averaged fluxes attributed to the most long- and short-lived cyclones become more comparable (dashed lines in Fig. 8c), which results in a ratio around two

(Fig. 8d). Similarly, the ratio between the most and least intense cyclones (dotted lines) is reduced compared to the accumulated fluxes but still lies well above five around $50°$ S. Thus, strongly intensifying (or intense) cyclones contribute more the zonal mean MSE fluxes because the attributed instantaneous fluxes are greater and not because these cyclones are more long-lived.

The average cyclone-attributed MSE flux of all SH cyclones, calculated at $50°$ S, is $0.12\,\mathrm{PW}$ (black dashed line in Fig. 8c). During each winter season, around 340 unique cyclones are identified. These have an average lifetime of 3.4 days, such that 12.5 cyclones are present at an instant on average[4]. The estimated $1.5\,\mathrm{PW}$ that they contribute altogether matches the seasonal mean flux shown in Fig. 7a.

An intriguing side result is that the lifetime-averaged cyclone-related MSE flux is larger when computed using all cyclones than when using only the longest or shortest life cycles (black line in Fig. 8c). This could be explained by the fact that long-lived cyclones have a long weakening phase without large fluxes, whereas short systems do not intensify very strongly.

A key finding is that the intense cyclones contribute more flux to the zonal integral than the cyclones that intensify most rapidly, despite comparable near-cyclone fluxes in the composites (Fig. 5). One explanation is that the most intense cyclones cover a larger area than those that intensify the most strongly. Earlier studies suggest that cyclone size is more closely related to the intensity than to the intensification rate (Rudeva and Gulev, 2007). Consequently, there is more cyclone-attributed flux located further downstream of the cyclone center (not shown), and as a result a larger contribution to the zonal integral by the most intense cyclones.

A comprehensive sensitivity analysis ensures the robustness of the findings presented above. The results are neither sensitive to measuring the intensification rate in $\mathrm{Bergeron}$ instead of six-hourly changes in SLP along a track (Sanders and Gyakum, 1980), nor to defining intensity using SLP anomalies from local climatology rather than absolute SLP values (Cornér et al., 2025). The only noteworthy difference is, as expected, that the latitudinal offset between the peaks of the attributed fluxes of the deepest and weakest cyclones is reduced when using SLP anomalies. When using absolute SLP, this offset is also reduced when sub-selecting cyclones intensifying only within 50–$60°$ S. As a result, the fluxes attributed to the most intense cyclones remain $\approx 50\,\%$ higher compared to those of the most strongly intensifying ones. Excluding tracks shorter than $3\,\mathrm{d}$ further ensures that weak, short-lived tracks do not distort the picture. Thus, the large ratio between intense and weak cyclones (dotted line in Fig. 8) is not an artifact of the poleward climatological SLP decrease. Qualitatively, the results are also not sensitive to the parameter choices of the applied decomposition method or flux attribution threshold (the interested reader is referred to Appendix Fig. D3).

In summary, against expectations based on the composite analysis presented in Sect. 3, the fluxes attributed to intense cyclones contribute more strongly to the zonal integral compared to those attributed to the most rapidly intensifying cyclones. Thus, not only the intensification rate but also the spatial extend of cyclones, which is typically large for the most intense cyclones, is an important determinant of the zonally integrated poleward energy transport associated with extratropical cyclones.

[4] 340 cyclones / $92\,\mathrm{d} \times 3.4\,\mathrm{d}$.

5 The relationship between the seasonal mean transient MSE flux and seasonal cyclone numbers

Finally, we investigate the relationship between extratropical cyclones and the zonally and vertically integrated transient MSE flux, $\langle[v'm'_{\mathrm{MA}}]\rangle$, on a seasonal scale. Given that large transient MSE fluxes can be attributed to strongly intensifying and intense cyclones, in this section it is examined how the seasonal number of these storms relates to the seasonal mean zonally integrated transient MSE flux and, ultimately, the total atmospheric heat transport. The seasonally averaged transient MSE flux attributed to cyclones is denoted with $\langle[\overline{v'm'}^{\mathrm{cycl}}_{\mathrm{MA}}]\rangle$ as above. In the following, focus is laid on the latitude of $50°$ S which corresponds to the peak of the cyclone-attributed transient MSE fluxes (Fig. 7a). The classification of cyclones as 'strong', 'moderate', and 'weak' follows Sect. 2.4.

5.1 Seasonally averaged transient MSE fluxes and cyclone numbers

At $50°$ S, cyclones that intensify strongly account for around $43\,\%$ of the cyclone-related transient MSE flux in a season, i.e., $\langle[\overline{v'm'}^{\mathrm{cycl}}_{\mathrm{MA}}]\rangle$ (yellow box in Fig. 9). This fraction is slightly higher for the intense cyclones ($\approx 47\,\%$). For moderately intense cyclones and moderately intensifying cyclones (defined from the 25$^{\mathrm{th}}$ to 75$^{\mathrm{th}}$ percentile), the fractional contributions lies within the $40-50\,\%$ range (grey boxes in Fig. 9). Their contribution to the seasonal mean heat transport is therefore comparable to the strong and strongly intensifying cyclones, although they are (on average) twice as numerous. In turn, weak and weakly intensifying cyclones only account for less than $15\,\%$ of the attributed fluxes in a season.

The above results may suggest an almost linear relationship between intensification rate and transient MSE flux: In the case of a linear relationship, one would expect the cyclones above the 75$^{\mathrm{th}}$ percentile to contribute approximately $44\,\%$ to the budget.[5] The flux indeed increases with cyclone intensification rate and intensity. However, for cyclones intensifying very rapidly the relationship is found to be non-linear, while it is rather exponential for intensity (not shown). Further, the intensities are not equally distributed but follow a (skewed) normal distribution for both characteristics. In sum, the identified fractions mean that the strongest cyclones contribute disproportionally compared to their frequency, which agrees with the conclusions in Messori and Czaja (2015). Yet, despite the large contribution to the zonal budget by the strong cyclones, more than half of the seasonal $\langle[\overline{v'm'}^{\mathrm{cycl}}_{\mathrm{MA}}]\rangle$ results from moderate cyclones. This suggests that the number of strong cyclones has only a weak control on the zonally-integrated seasonal mean budget of transient MSE flux that can be associated with extratropical cyclones.

Indeed, the seasonal zonally and vertically integrated transient MSE flux attributed to cyclones, $\langle[\overline{v'm'}^{\mathrm{cycl}}_{\mathrm{MA}}]\rangle$, is not highly correlated with either the number of *strongly intensifying* or the number of *intense* cyclones (Fig. 10b and c). However, $\langle[\overline{v'm'}^{\mathrm{cycl}}_{\mathrm{MA}}]\rangle$ is correlated with *total* cyclone number (Fig. 10a).

It was found that when omitting the flux attribution and simply correlating the total number of cyclones with the mean transient MSE flux ($\langle[\overline{v'm'}_{\mathrm{MA}}]\rangle$), the correlation remains positive albeit weaker than the previous result based on the cyclone-attributed flux (cf. Fig. 10a and d). $\langle[\overline{v'm'}_{\mathrm{MA}}]\rangle$ is not correlated with the number of most rapidly intensifying cyclones (Fig. 10e) but is correlated with the number of the most intense cyclones (Fig. 10f). The latter is larger compared to the case with flux attribution (c.f. Figs. 10c and f). Under the assumption that the most intense cyclones dominate the overall transient MSE flux,

[5] This result can be conveniently confirmed using the arithmetic series.

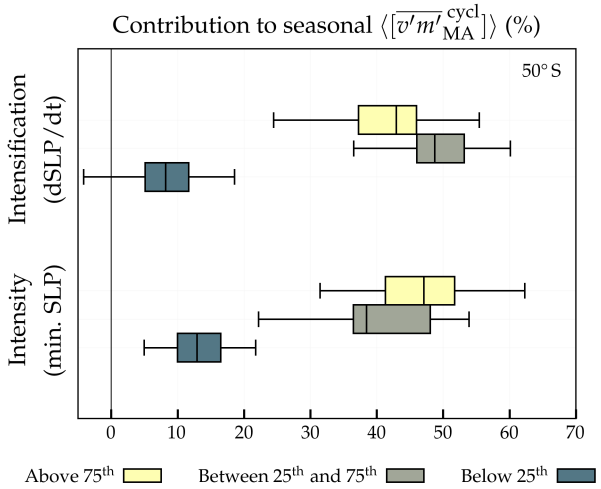

Figure 9. Contributions of cyclones within three different ranges of intensification rate (top) and intensity (bottom) to the seasonal transient MSE flux that is attributed to cyclones ($\langle[\overline{v'm'}^{\text{cycl}}_{\text{MA}}]\rangle$). For each life cycle characteristic, cyclones are grouped seasonally by the 25$^{\text{th}}$ and 75$^{\text{th}}$ percentiles derived from the climatological sets of cyclones that have non-zero $\langle[\overline{v'm'}^{\text{cycl}}_{\text{MA}}]\rangle$ at this latitude. The seasonal fluxes attributed to the cyclones that lie above the 75$^{\text{th}}$ percentile are represented in yellow, the ones between the 25$^{\text{th}}$ and 75$^{\text{th}}$ in grey, and the ones below the 25$^{\text{th}}$ in blue. Medians are shown with solid lines within the boxes that denote the interquartile range. Whiskers indicate 1.5 times the interquartile range while values outside of this range are not shown. MSE fluxes and cyclone numbers correspond to 50° S.

the decrease of the correlation from Fig. 10f to Fig. 10c could be an indication that the attribution method does not perfectly attribute MSE fluxes to cyclones. One possible explanation is that the attribution method attributes some fluxes of the most intense cyclones to neighboring weaker ones. This would be in line with the fact that the correlation of the cyclone-attributed fluxes with the overall cyclone number (Fig. 10a) is higher than with the intense ones (Fig. 10c). Over a season, more cyclones with MSE fluxes attributed independently of intensity would be expected to have more attributed MSE flux overall.

While this analysis suggests that on a seasonal scale $\langle[\overline{v'm'}^{\text{cycl}}_{\text{MA}}]\rangle$ relates to the number of all cyclones, n_{all}, and $\langle[\overline{v'm'}_{\text{MA}}]\rangle$ is driven by the number of intense cyclones, n_{intense},[6] these correlations vary substantially with flux attribution percentile and flux decomposition method in both cases (Fig. E1b,h). These analyses are also carried out defining transient MSE fluxes from high-pass filtered fields (HP) and, separately, from zonal anomalies (ZA). For the flux attributed using percentile rank $p = 0.9$, the correlation between the cyclone-attributed fluxes and the number of all cyclones, $\rho\left(\langle[\overline{v'm'}^{\text{cycl}}_{\text{HP}}]\rangle, n_{\text{all}}\right)$, equals 0.39, while $\rho\left(\langle[\overline{v^*m^*}^{\text{cycl}}_{\text{ZA}}]\rangle, n_{\text{all}}\right) = 0.70$ (Fig. E1b). Similarly, the correlation between overall transient MSE fluxes and the number of intense cyclones, $\rho\left(\langle[\overline{v'm'}_{\text{HP}}]\rangle, n_{\text{intense}}\right)$, is at least 0.65, whereas $\rho\left(\langle[\overline{v^*m^*}_{\text{ZA}}]\rangle, n_{\text{intense}}\right) \leq 0.27$ (Fig. E1h). Given the large fraction of flux attributed to the cyclone sets of moderate intensity (or intensification, Fig. 9), it is not surprising to find low correlations with the number of intense (or strongly intensifying) cyclones. The method dependency, however, was not expected, and the physical mechanisms governing it are discussed in Sect. 6.2.

[6] In both cases, the slope of the linear fit is significantly different from zero as indicated by the p-values on the panels (using a two-tailed test, Fig. 10a,f).

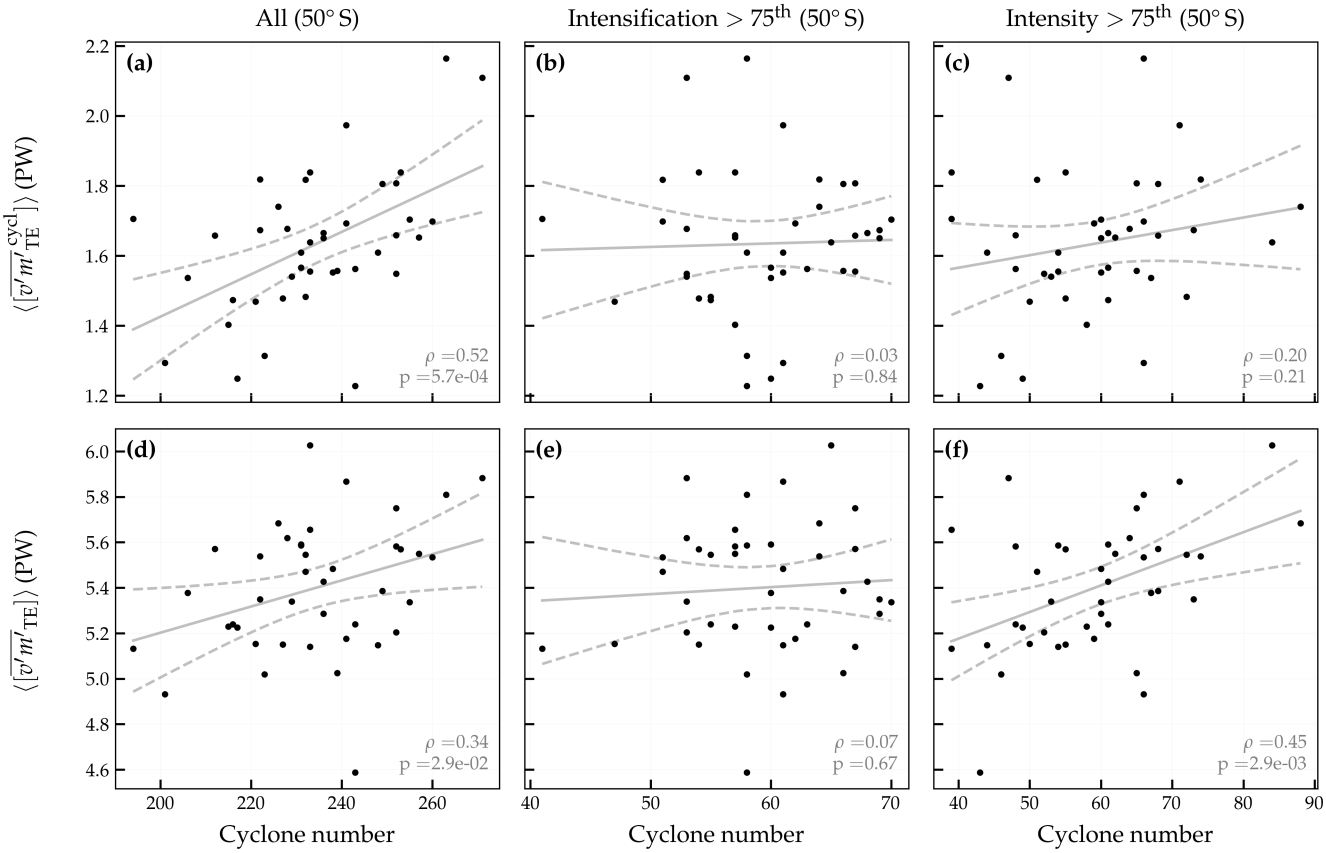

Figure 10. Relationship between seasonally averaged transient MSE flux and cyclone numbers for SH JJA at 50° S. **(a)** The cyclone-attributed transient MSE flux $\langle[\overline{v'm'}^{\text{cycl}}_{\text{MA}}]\rangle$ (units of PW) and the number of all cyclones with $\langle[\overline{v'm'}^{\text{cycl}}_{\text{MA}}]\rangle \neq 0$ at that latitude. **(b, c)** as **(a)** but for the number of strongly intensifying cyclones and intense cyclones, respectively. **(d)–(f)** as **(a)–(c)** but for the overall transient flux $\langle[\overline{v'm'}_{\text{MA}}]\rangle$. The grey solid line represents a best estimate of a linear fit and dashed grey lines the corresponding confidence band. Correlation (ρ) and p-value of the slope of the linear fit (p) are indicated in each panel.

5.2 Cyclone numbers and total heat transport

On the six-hourly timescale, the transient eddy and overturning circulations are temporally anti-correlated in the midlatitudes (Cox et al., 2024b). One could argue that the splitting into transient eddy and mean overturning circulation is therefore not strictly related to circulation features (e.g., surface (anti-)cyclones, troughs, and ridges), which naturally contain signals from eddy and mean components because the mean was computed including the eddies in the first place. Thus, we also investigate the total heat transport, $\langle[\overline{vm}]\rangle$ (the left-hand side of Eq. 2), instead of the transient eddy MSE flux. We continue to count cyclones as above using the latitudinal extent of their attributed transient MSE fluxes.

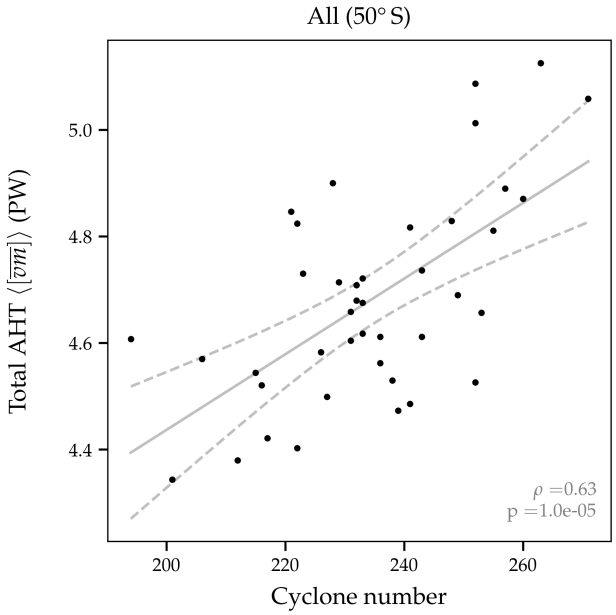

Figure 11. Relationship between seasonally averaged, zonally integrated total heat transport, $\langle[\overline{vm}]\rangle$, at $50°$ S (PW) and number of cyclones with a non-zero transient MSE flux attributed to them ($\langle[\overline{v'm'}^{\text{cycl}}_{\text{MA}}]\rangle \neq 0$) at the same latitude. Grey solid and dashed lines as in Fig. 10. The correlation (ρ) and the p-value of the slope of the linear fit (p) are indicated on the panel.

For the total heat transport at $50°$ S, the correlation with the total cyclone number of cyclones passing through this latitude is 0.63. Of the latitude bands tested, $50°$ S is the latitude where this correlation is largest (Fig. E2j). The decrease towards the pole is not fully understood but potentially is connected to the increasing importance of planetary-scale relative to synoptic-scale related MSE fluxes that increases towards the pole (Stoll et al., 2023). Note that when simply taking the number of all cyclones in the entire SH instead of the number of cyclones only at $50°$ S the correlation reduces. This suggests that capturing the latitudinal extent of cyclones as shown in Fig. 2 is important.

To sum up, no robust relationship between the seasonal number of intense or strongly intensifying cyclones and the seasonal transient MSE flux is identified. In contrast to the transient flux, the seasonal mean of the total zonally integrated MSE flux at $50°$ S exhibits a more robust correlation of $0.40 - 0.64$ with the number of all cyclones passing that latitude. The correlation range results from the degrees of freedom in the counting method (cf. Fig. 2).

6 Summary and conclusions

6.1 Key findings

This study examines the relationship between zonally integrated heat transport and life cycle characteristics of extratropical cyclones during SH winter (JJA) using the ERA5 reanalysis. We have developed a novel method that combines the vertically integrated transient eddy MSE flux with a feature-based cyclone tracking scheme. Specifically, the three central objectives of this study are: (i) to reveal the temporal evolution of the local meridional transient MSE fluxes during the cyclone life cycles; (ii) to quantify the contributions of cyclones to the zonally integrated transient MSE flux and assess how the contributions of individual cyclones vary depending on life cycle characteristics such as lifetime and intensification rate, and; (iii) to explore the relationship between cyclone numbers and heat transport on the seasonal scale. In the following, the key findings are summarized.

- Locally, the meridional transient MSE fluxes peaks during the intensification phase and declines before the cyclone reaches its mature stage (Fig. 3), which is in agreement with the theory of baroclinic growth (as is the vertical structure of the fluxes). Cyclone-centered composites reveal large poleward MSE fluxes located in the warm sector confined between the warm and cold fronts and a smaller peak in the cold sector (Fig. 4). Furthermore, there is a clear positive (although nonlinear) relationship between the strength of the transient MSE flux and the growth rate and maximum intensity of cyclones (Fig. 5). Crucially, a non-negligible fraction of warm-sector and cold-sector fluxes are located outside of the cyclone masks defined by closed SLP contours. Typically, warm-sector fluxes extend further equatorward and are spatially bound by the frontal zones. The poleward flux of latent heat is, as expected, confined to the warm sector which leads to an increasing contrast between warm-sector and cold-sector MSE fluxes towards the equator (Fig. 6).

- In the zonal integral, the novel attribution method based on feature overlap attributes $30\,\%$ of the transient MSE flux to cyclones. This method places the latitudinal maximum in cyclone attributed MSE flux closer to the overall transient MSE flux relative to only counting the MSE flux within cyclone masks (Fig. 7). This supports the notion that MSE fluxes associated with warm conveyor belts, which are located typically along the boundaries and outside of the cyclone masks, are important contributors to zonally integrated MSE transport proposed in Messori and Czaja (2015). The most intense cyclones have the largest fluxes attributed to them (Fig. 8). The attributed fluxes also increase with cyclone intensification rate. As expected, the accumulated fluxes increase with cyclone lifetime but cyclone lifetime is a much weaker indicator for the attributed flux than intensity or intensification rate. Previous research has found that the poleward propagation speed (and not necessarily intensity) is the characteristic for which the poleward moisture fluxes within a fixed radius around the center are the largest (Sinclair and Dacre, 2019). For MSE fluxes in this study, the cyclones with fastest poleward propagation speed show comparable lifetime-averaged fluxes to those of the most intense cyclones at some latitudes but not consistently larger ones (not shown).

- The identified link between cyclone intensity and attributed transient MSE fluxes also applies to the seasonal scale. Storms that have an intensity larger than the 75^{th} climatological percentile collectively contribute to around $45\,\%$ of the

seasonally integrated cyclone-attributed heat transport (Fig. 9). The intense cyclones thereby transport roughly as much transient MSE flux as the moderately intense cyclones despite the latter being, on average, twice as numerous. However, the fraction of the MSE flux associated with the intense cyclones are not disproportionate enough so that their number alone does not shape the seasonal mean transient flux (Fig. 10). This also holds true for cyclone intensification and is further discussed below. For the total heat transport at 50° S, the correlation with the number of all cyclones at that latitude lies between 0.40–0.64 (Figs. 11 and E1j). However, the correlation is reduced at other latitudes (Fig. E2j) such that further research is needed to better understand whether changes in cyclone numbers can be related to atmospheric heat transport changes constrained by the Earth's energy imbalance.

The determined contributions of extratropical cyclones to the total heat transport are summarized in Fig. 12: Cyclones contribute to the high-frequency (or 'transient') eddy heat transport which, depending on the flux decomposition, is accompanied by low-frequency (or 'stationary') background fluxes and the mean overturning circulation. The high-frequency eddy MSE fluxes attributed to cyclones can be linked to different subsets of cyclones based on their intensity or intensification rate. Other high-frequency eddy MSE fluxes not attributed to cyclones may occur far from the cyclone center (possibly along fronts), be linked to high pressure systems, or be unrelated to weather features with closed contours such as meandering zonal flows.

6.2 On the choice and influence of eddy-mean decompositions

In the above summary, the conclusions are overall independent of the choice of eddy-mean decomposition method. A consequential method dependence in our study was only found for the correlation between the seasonal cyclone number and the transient MSE flux (Sect. 5 and Appendix E). This points to a non-negligible influence of planetary, low-frequency waves to the local transient MSE flux attributed to individual systems as discussed below (Messori and Czaja, 2014; Stoll et al., 2023). Because some fraction of this background flux is attributed to an individual extratropical cyclone, the effect of its life cycle characteristics on the zonally integrated flux is partly masked. For large enough sample sizes, this method-dependency averages out (N $\gtrapprox 200$ as in Sects. 3 and 4), but the effect influences the result when considering a seasonal set of intense cyclones (N ≈ 60, Sect. 5).

When high-pass filtering, a wave-like signal with a frequency $\sim (11\,\mathrm{d})^{-1}$ is filtered out whereas in the zonal anomaly framework the corresponding flux is partly attributed to cyclones. It is found that the number of intense cyclones modulates the high-pass filtered transient flux,, while it does not determine the transient flux computed from zonal anomalies (Fig. E1d,h). We argue that the lower correlation for the zonal anomaly method arises because part of the background flux is attributed to each cyclone — independently of cyclone intensification rate or intensity. Conversely, the addition of this background signal leads to a higher correlation between the seasonal fluxes and the *overall* cyclone number (Fig. E1b,f). The monthly anomaly framework is a special case with the amount of background flows attributed to cyclones lying somewhere between the other two methods. As a result, the correlations broadly fall within the two other methods (Fig. E1).

Our results may suggest that high-pass filtering is the most suitable decomposition method to investigate the energy transport footprint of extratropical cyclones. While the choice of the cut-off frequency (or likewise the spatial wavenumber) can be

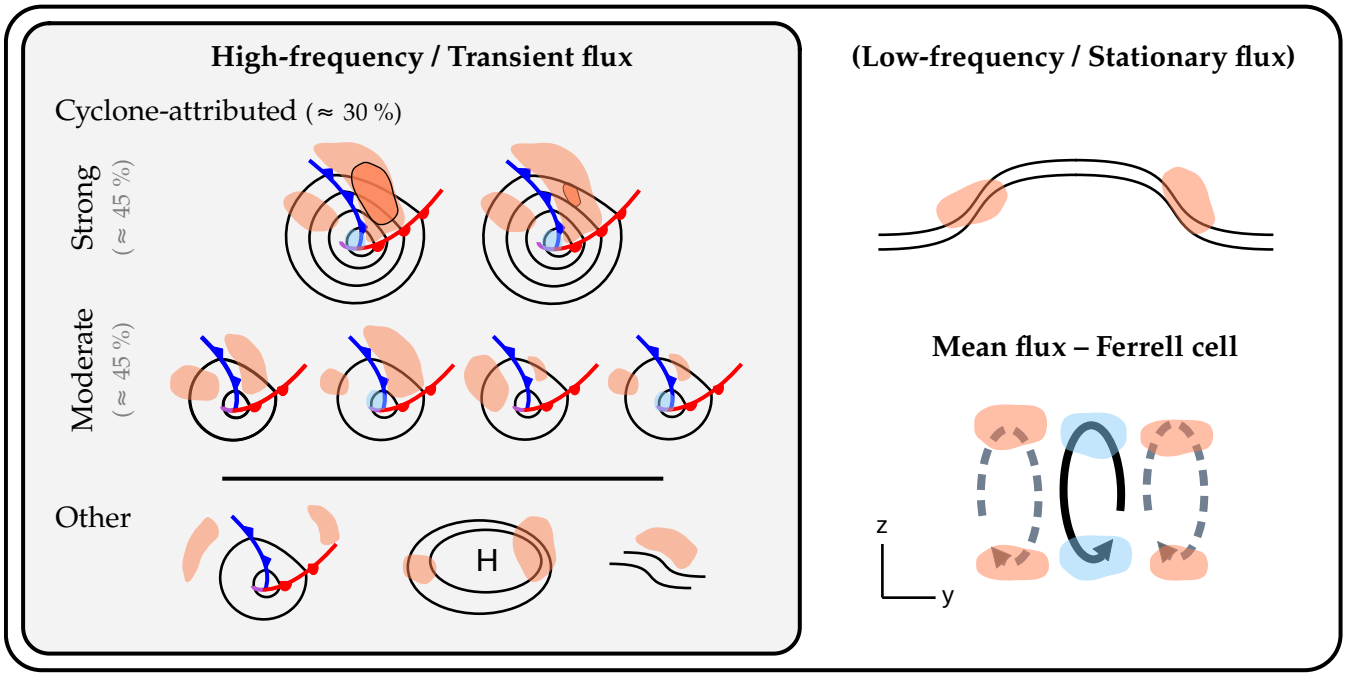

Figure 12. Schematic of the decomposition of total atmospheric heat transport into different flux components and contributions by extratropical cyclones: When adopting an eddy-mean decomposition, the heat transport is the sum of a high-frequency, transient eddy flux component, potentially a separate low-frequency or stationary eddy component, and the flux related to the mean overturning circulation. Orange and blue shading denotes poleward and equatorward meridional MSE fluxes, respectively. The high-frequency, transient eddy fluxes are further split into cyclone-attributed (≈ 30 % of the high-frequency eddy fluxes) and other fluxes. Surface cyclones in the left box are illustrated by SLP contours that are accompanied by warm fronts (red lines), cold fronts (blue), and occlusions (purple). 'Strong' and 'moderate' refer to the intensity or intensification rate of cyclones with 'weak' cyclones omitted. Grey percentage indications refer to the approximate contribution of those cyclones to the cyclone-attributed eddy MSE flux (and not the overall high-frequency eddy flux). Low-frequency or stationary flow is sketched by wave-like black lines in the top right. In the bottom right, the zonal mean flux is drawn in a latitudinal and vertical y-z cross-section with the overturning circulation illustrated with solid black (Ferrell cell) and dashed grey (Hadley and polar cells) arrows.

motivated dynamically (e.g. Eady, 1949), some spectral power of a warm conveyor belt, for instance, is contained in the flow that is filtered out. As the spectrum of total heat transport is predominantly continuous (see for instance supplementary of Stoll et al., 2023), choosing a scale separation in time or space is a balance between how much low wavenumber flux is attributed to a background component and how much of it imprints in the transient eddy component, eventually near individual cyclones. Note that high-pass filtering is the method with the smallest fraction of total heat transport explained by cyclone-attributed transient MSE flux (Fig. D1). Closing the atmospheric heat budget (Eq. 1) using such an approach can require computing many cross-terms (Franzke and Harnik, 2023). Thus, the choice of eddy-mean decomposition method depends on the research question.

6.3 Further remarks

Note that the contribution of low-frequency and planetary-scale waves to the zonally integrated heat transport likely increases with height Stoll et al. (2023). Focusing on surface cyclones, one possible extension of this work is a repetition of the above analyses using only low-level fluxes. In addition to reducing the above sensitivity with respect to the definition of what is background flux, this would also segregate stratospheric contributions unrelated to surface weather. In the SH, we do not expect a strong influence of stratospheric fluxes on our results; at 65° S, stratospheric fluxes account for only $11\,\%$ of the column-integrated fluxes explaining $10\,\%$ of its variance (Cardinale et al., 2021).

While our analysis focused on SH winter, technically, the methods can readily be applied to the NH and other seasons as well. Yet, in the NH the stationary signal is much larger, which increases the sensitivity with respect to the flux decomposition method (not shown) and weakens the connection between heat transport by cyclones and hemispheric scale radiative budget constraints. Furthermore, one has to reflect on whether and how to disentangle the signals arising from the Atlantic and Pacific basins due to different changes in cyclone characteristics. The response of the cyclone number to warming and storm track latitude, for instance, is different in these two basins (e.g. Seiler and Zwiers, 2016; Chang, 2018). Moreover, stratospheric contributions to the vertical integral are larger in the NH (Cardinale et al., 2021) such that one should consider a sensitivity analysis with respect to the vertical integration bound.

More sophisticated methods for attributing different kinds of fluxes to cyclones (e.g., Fearon et al., 2021; Lopez-Marti et al., 2025) are conceivable. Warm and cold sector MSE fluxes could be identified using atmospheric river (Shields et al., 2018) or warm conveyor belt masks (Heitmann et al., 2024) and cold sector masks (Zolina and Gulev, 2003; Kolstad and Bracegirdle, 2008; Vannière et al., 2016), respectively. Note that depending on the identification method, warm conveyor belt masks might require computing Lagrangian air parcel trajectories (Heitmann et al., 2024). A different approach to capture the heat transport along the fronts could be to attribute fluxes via identified surface fronts (e.g., as in Papritz et al., 2014), although it is unclear how well these capture fluxes throughout the sectors (Messori et al., 2017). Instead of attributing fluxes to cyclones, one could directly study the influence of warm conveyor belt and cold sector numbers on the zonal energy budget. Since fluxes do not peak near the center of weather systems but rather between cyclones and anticyclones, that would make the question about the contribution of anticyclones obsolete (Ruggieri et al., 2020).

This study has not addressed trends in either MSE fluxes or cyclone numbers. The decrease of SH winter cyclones in a warmer climate, however, motivates further research on the relationship between extratropical cyclones and zonal mean energetics. A follow-up study is planned applying there here developed diagnostics to idealized and fully-coupled climate simulations.

Code and data availability. The underlying ERA5 reanalysis data can be downloaded from https://doi.org/10.24381/cds.bd0915c6 (Hersbach et al., 2020). A code repository to reproduce the data and the figures and a data archive are in preparation and will be made accessible upon publication.

Table A1. List of abbreviations used in this study.

Abbreviation	Meaning
DJF	December, January, February
EQ	Equator
HP	High-pass (filtering method, framework)
JJA	June, July, August
(r)lat	(rotated) latitude
(r)lon	(rotated) longitude
MA	Monthly anmoaly (framework)
MSE	Moist static energy
NH	Northern Hemisphere
SFA	Standardized flux anomalies
SH	Southern Hemisphere
SLP	Sea level pressure
SP	South Pole
TOA	Top of atmosphere
ZA	Zonal anomaly (framework)

Appendix A: Abbreviations and terminology

To facilitate the lecture of this study, a list of abbreviations (Table A1) and frequently used mathematical terms (Table A2) is provided.

Appendix B: Further details on the MSE flux attribution to cyclones

In our study, we identify events of large eddy MSE fluxes based on a seasonally and latitudinally varying flux threshold. This threshold is computed by aggregating all values of a latitude band of the same time of every year and computing a percentile based on that distribution. This is illustrated in Fig. B1. The identified features are then attributed to surface cyclones using SLP-derived masks as shown in Fig. 2. The transient MSE fluxes differ for each flux decomposition method (Fig. B2a–c) and so do the identified flux features (Fig. B2d–f). As a result, at a single instance a cyclone may be attributed some equatorward flux of positive MSE (dark blue patches at 60° E in Fig. B2g,h) or not (Fig. B2i). Note that not all flux features overlap with cyclone masks (yellow patches in Fig. B2g–i).

Table A2. Description of selected terms used in this study. Subscripts of eddy fluxes change in accordance with dashes and asterisks.

Term	Description
$v'm'_{\mathrm{MA}}$	Meridional transient MSE fluxes derived from monthly anomalies
$v'Lq'_{\mathrm{MA}}$	Meridional transient moisture fluxes derived from monthly anomalies
$v'm'_{\mathrm{HP}}$	Meridional transient MSE fluxes derived from high-pass filtering
$v^*m^*_{\mathrm{ZA}}$	Meridional transient MSE fluxes derived from instantaneous anomalies from the zonal mean
$[v'm'_{\mathrm{MA}}]$	Zonal mean (or zonally integrated) transient MSE fluxes
$\overline{v'm'}_{\mathrm{MA}}$	Monthly or seasonal mean transient MSE fluxes
$\langle v'm'_{\mathrm{MA}}\rangle$	Vertically integrated transient MSE fluxes
$\langle[v'm'_{\mathrm{MA}}]\rangle$	Vertically integrated zonal mean (or zonally integrated) transient MSE fluxes
$\langle[\overline{v'm'}_{\mathrm{MA}}]\rangle$	Seasonal mean zonally and vertically integrated ('overall') transient MSE fluxes
$\langle v'm'^{\mathrm{cycl}}_{\mathrm{MA}}\rangle$	Vertically integrated transient MSE fluxes attributed to cyclones
$\langle[v'm'^{\mathrm{cycl}}_{\mathrm{MA}}]\rangle$	Zonal integral of vertically integrated transient MSE fluxes attributed to cyclones
$\langle[\overline{v'm'}^{\mathrm{cycl}}_{\mathrm{MA}}]\rangle$	Seasonal mean zonal integral of vertically integrated transient MSE fluxes attributed to cyclones
$\langle[\overline{vm}]\rangle$	Seasonal mean ('total') heat transport
$v'm'^{\mathrm{clim}}_{\mathrm{MA}}$	Climatology of meridional transient MSE fluxes
$\langle[\overline{v'^{,*}m'^{,*}}_{\_\_}]\rangle$	Seasonal mean zonal and vertical integral of 'overall' transient, cyclone-attributed MSE fluxes for a given framework
$\langle[\overline{v'^{,*}m'^{,*}}^{\mathrm{cycl}}_{\_\_}]\rangle$	Seasonal mean zonal integral of vertically integrated, cyclone-attributed transient MSE fluxes for a given framework
n_{all}	Seasonal number of cyclones that were attributed non-zero transient MSE flux at a latitude band of interest

Appendix C: Sensitivity and variability of near-cyclone eddy MSE fluxes

To further strengthen the conclusions drawn from the cyclone composites, a significance test is performed for the monthly anomaly framework. For this we address the standardized flux anomalies (SFA) from the climatological seasonal mean, $v'm'^{\mathrm{clim}}_{\mathrm{MA}}$, defined as

$$\mathrm{SFA}(lon, lat, time, pressure) = \frac{v'm'_{\mathrm{MA}}(lon, lat, time, pressure) - v'm'^{\mathrm{clim}}_{\mathrm{MA}}(lon, lat, pressure)}{\sigma(v'm'_{\mathrm{MA}})(lon, lat, pressure)} \tag{C1}$$

with σ the standard deviation over the climatological period. Locations in the composite where mean(SFA) $= 0$, we regard the $v'm'_{\mathrm{MA}}$ of the individual events that we used for compositing as not significantly different from climatological $v'm'_{\mathrm{MA}}$ fluxes. In other words, the null hypothesis, mean(SFA) $= 0$, is rejected if within the composite, fluxes are sampled that are on average different from climatology. We perform a two-sided, one sample *t*-test at each composite grid-cell (Fig. C1). Overall, the dynamical features that were identified in the composites are based on flux anomalies that on average are significantly different from zero. Note that low $v'm'_{\mathrm{MA}}$ can be significant in the composite as it is lower than climatology.

Compared to the monthly anomaly (MA) framework, it is also the intensification phase (and not the mature stage) during which fluxes are largest when adopting the high-pass (HP) and zonal anomaly (ZA) decompositions (not shown). A comparison of the fluxes at peak cyclone intensification reveals that at $850\,\mathrm{hPa}$, high-pass filtered fluxes are marginally lower than MA

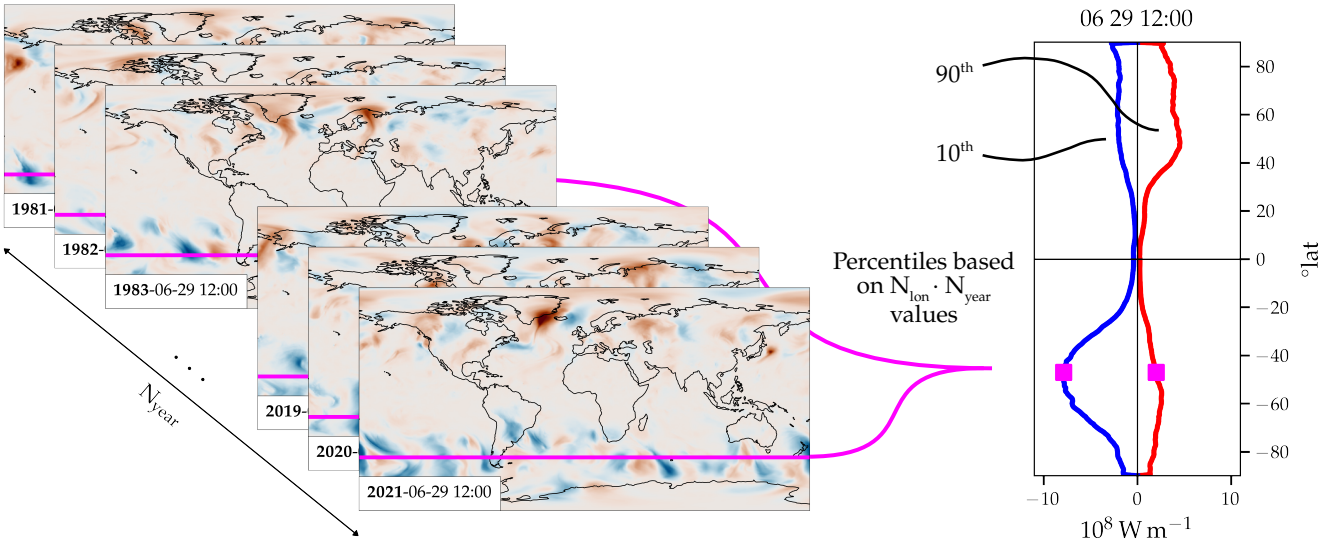

Figure B1. Illustration of the determination of the percentile threshold for eddy MSE flux events based on the monthly anomaly framework: For every six-hourly time step of a year — 29 June, 12:00 UTC, for instance — eddy MSE flux thresholds for poleward and equatorward fluxes are calculated at each latitude. These are based on the values of that latitude band and every corresponding time of year during the analysis period. Thus, the sample size which the percentile is computed from is the number of years (N_{lon}) times the number of grid-cells at a latitude circle (N_{lon}). The 10th and 90th percentiles of the vertically integrated eddy MSE fluxes (color shading on the left panel) for 29 June, 12:00 UTC are shown on the right in blue and red, respectively. The latitude of 47° S is highlighted in magenta.

fluxes (Fig. C2a,b). Moreover, the contrast between warm and cold sectors is reduced in the ZA framework (Fig. C2c), which could be explained by strong warm sector anomalies raising the instantaneous zonal mean MSE such that cold sector anomalies become larger compared to the other methods. Note that for the NH, the differences between MA and ZA are more pronounced (not shown) due to the time-stationary signal being declared as SE flux (Eq. 2). These descriptions are also valid for vertically integrated fluxes (Fig. C2d–f).

Appendix D: Method dependence of zonally integrated cyclone-attributed MSE flux

The method sensitivity of the seasonal contributions to transient eddy MSE flux by cyclones, which was discussed in Sect. 4.1, is shown in Fig. D1. Choosing lower percentiles moves the peak of the attributed fluxes towards the equator because larger masks (warm sectors extending further equatorward than the cyclone mask) are more often attached (Fig. D1a,d,g,j). Higher percentiles reduce the absolute fractions, yet percentages at 50° S remain close to 20 % for $p = 0.95$ (yellow lines in Fig. D1b,e,h,k). The cause of the relatively reduced correlation around 60° S for the ZA framework (Fig. D1i) is not clear but might be related to the presence of planetary waves. A repetition with an upper integral bound of 500 hPa (Fig. D1l) suggests this signal arises from lower levels (and not stratospheric dynamics).

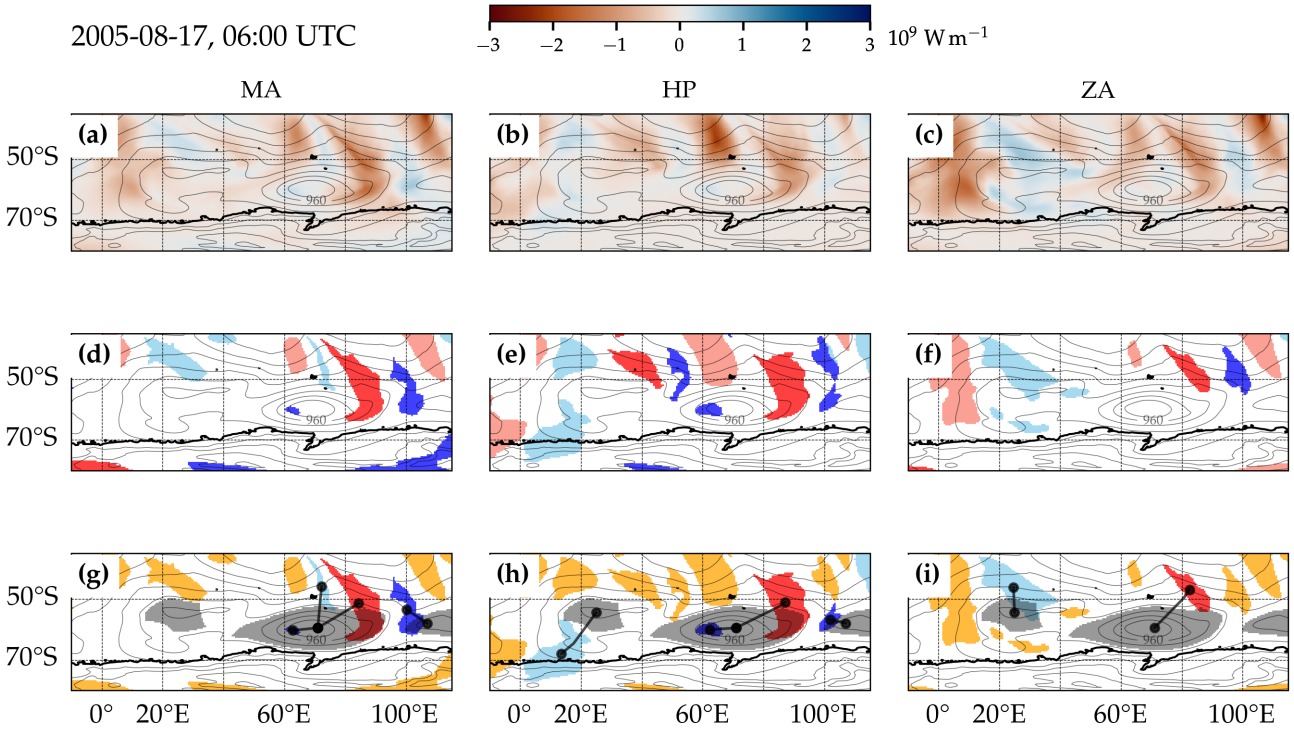

Figure B2. Snapshot of vertically integrated eddy MSE fluxes and their attribution to surface cyclones. **(a)** Vertically integrated eddy MSE fluxes calculated using the monthly anomaly framework (shading in $\mathrm{W\,m^{-1}}$) and SLP (black contours in steps of 10 hPa). **(b)** and **(c)** as in **(a)** but for the HP and ZA frameworks, respectively. **(d)–(f)** The binary masks corresponding to the identified flux features are shaded in reddish and bluish colors if MSE fluxes are poleward or equatorward, respectively, and in dark and light tones if fluxes correspond to positive and negative MSE anomalies, respectively. **(g)–(i)** In addition to above, surface cyclone masks are shown with grey patches. If flux features are not overlapping with cyclones, the features are colored yellow. Otherwise, black straight lines and dots indicate to which cyclones each feature is attributed to. Coastlines are depicted with black lines.

The averages depicted in Fig. 8 conceal the variability of the MSE fluxes attributed to individual cyclones. These are shown in Fig. D2 for the MA framework, in particular the cyclones that intensify least and most rapidly across the SH. While the means (solid lines) amount to around 20 PW, individual cyclones can be attributed more than 150 PW across a latitude band of more than 10°(Fig. D2a).

Regarding the method dependency of the zonally integrated MSE fluxes attributed to cyclones of different life cycle characteristics, the corresponding ratios of Fig. 8b,d are shown for lifetime-accumulated and lifetime-averaged fluxes in Fig. D3.

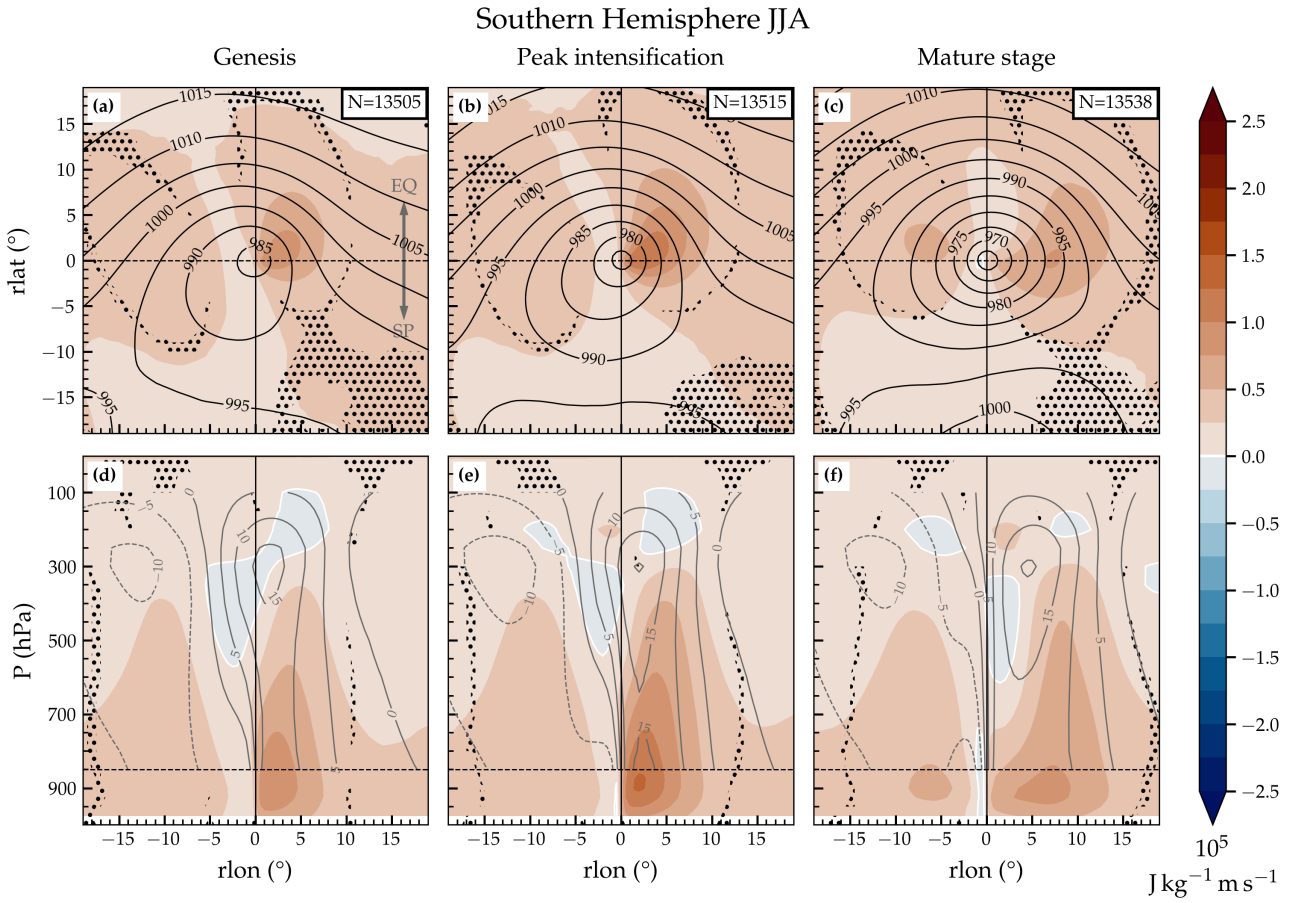

Figure C1. Statistical significance of composited transient MSE flux anomalies as in Fig. 4. Dotted areas indicate where the null hypothesis mean(SFA) $= 0$ (see Eq. C1) is not rejected at the 95 % confidence level. In **(d)–(f)**, grey contours indicate the (vertically sub-sampled) full meridional wind, v, as opposed to v' in Fig. 4d–f.

Appendix E: Sensitivity of the number–flux relationship to choice of flux decomposition method

While the relationships between different seasonal MA MSE fluxes and cyclone numbers are shown by scatter-plots (Fig. 10), for conciseness we only show the correlation values for the different flux decompositions and attribution percentiles. In addition to the relationships discussed in Fig. 10, we show correlations with the number of cyclones in the entire SH and with total heat transport ($\langle[\overline{vm}]\rangle$) for 50° S in the left column of Fig. E1 and different latitudes in Fig. E2. Note that measuring intensification rate in Bergeron and intensity based on SLP anomalies from a climatology instead does not yield a qualitatively different picture (not shown).

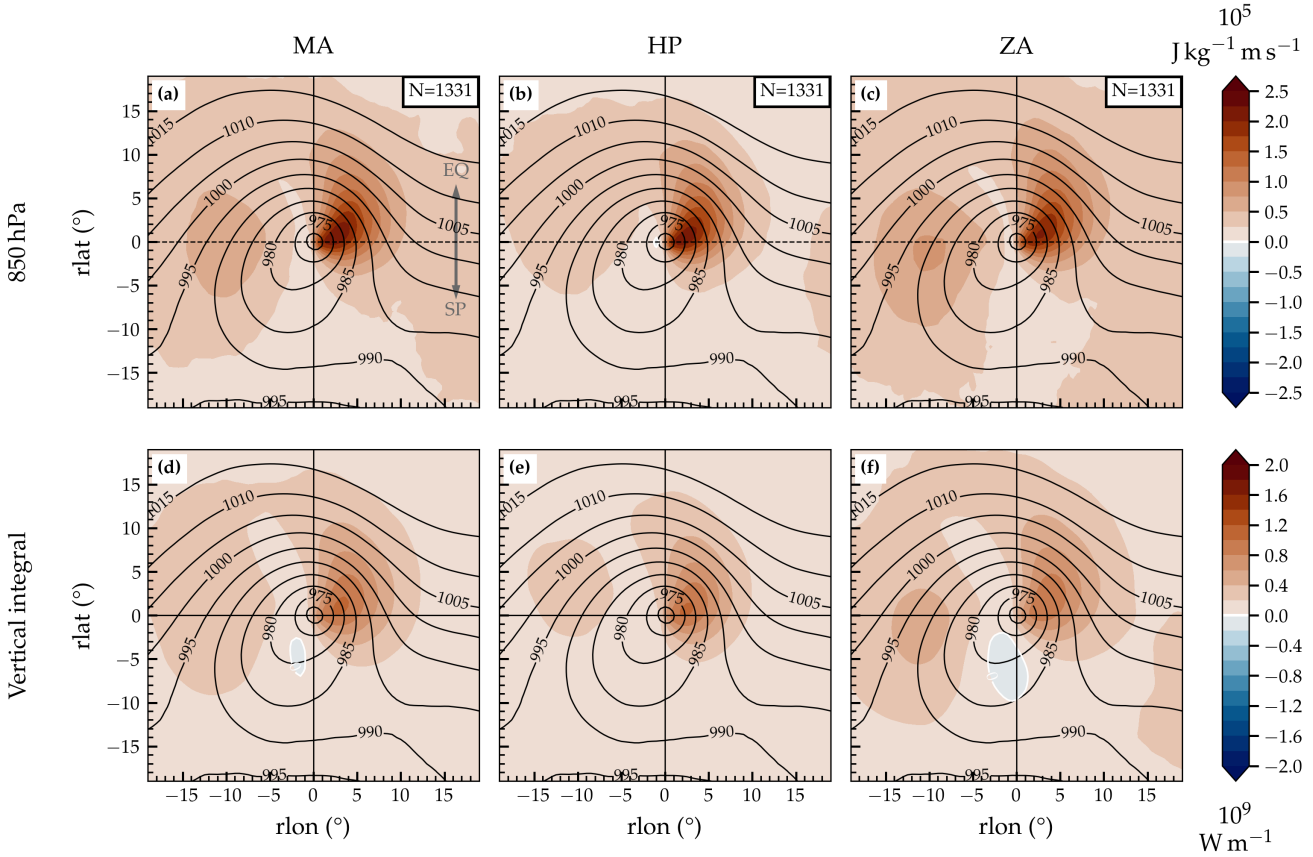

Figure C2. (a)–(c) Cyclone-centered eddy MSE flux at 850 hPa during time of maximum intensification for the 10 % most strongly intensifying SH cyclones during JJA for three different definitions of eddy flux (see method abbreviations in Sect. 1) in J m^{-1} kg s^{-1}. **(d)–(f)** Vertically integrated fluxes analogously to **(a)–(c)** but in units of W m^{-1}. Black contours indicate composite mean SLP in hPa. The number of cyclones in the composites are included in the upper right in panels **(a)–(c)**. A grey arrow is included for better orientation indicating directions of equator (EQ) and South Pole (SP).

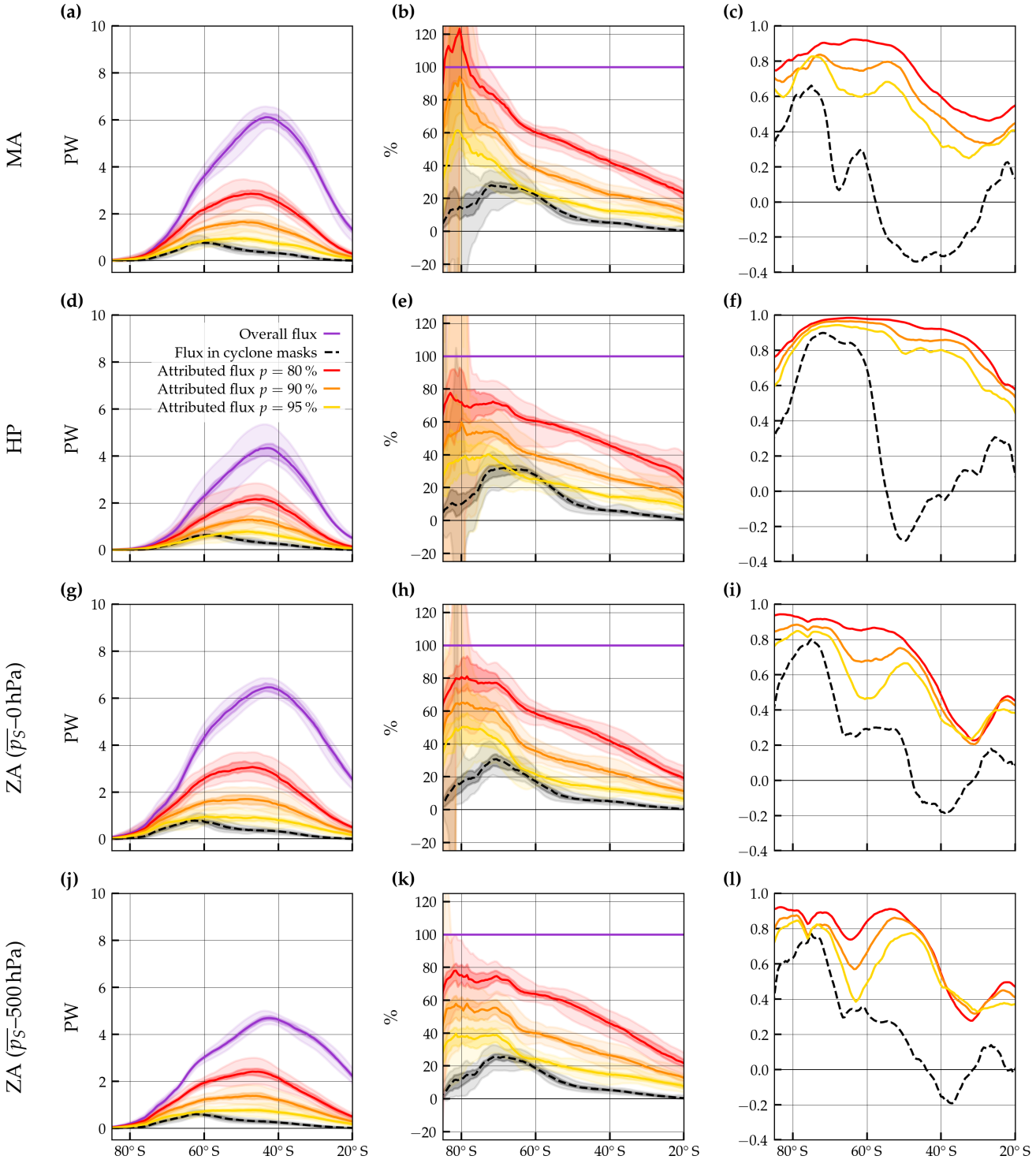

Figure D1. Same as Fig. 7 but repeated for different flux decomposition methods (see Sect. 2.3) and different percentile thresholds for attributing flux to cyclones (yellow, orange, and red distributions and lines corresponding to percentile ranks of 0.8, 0.9, and 0.95.

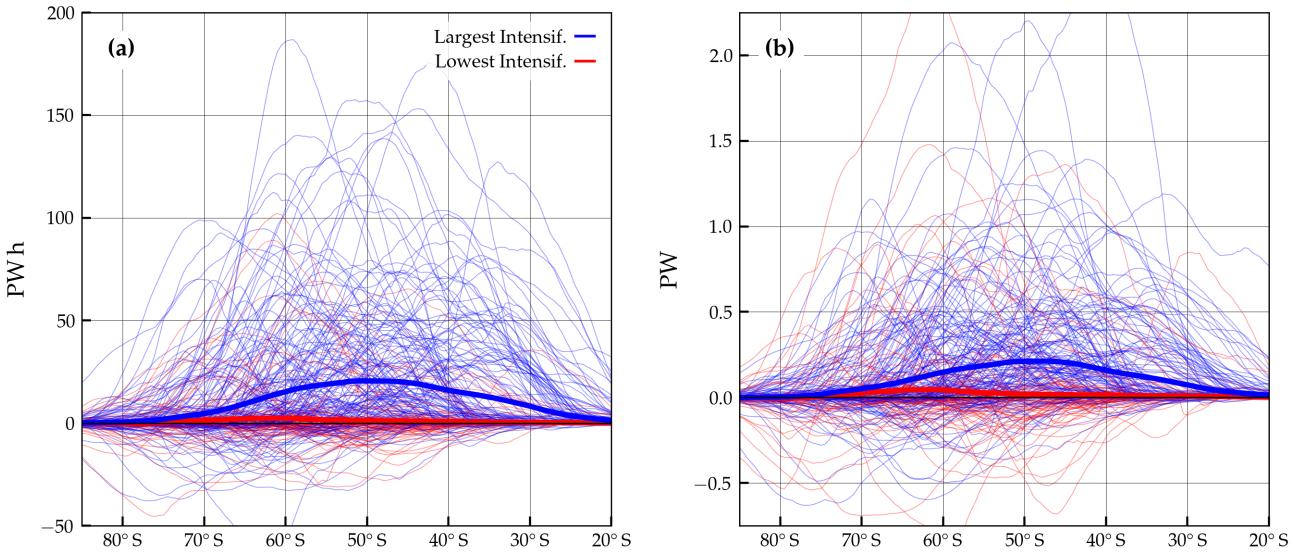

Figure D2. Zonally integrated transient MSE flux attributed to individual extratropical cyclones. **(a)** The lifetime-integrated flux (PW h) of the 200 most strongly intensifying cyclones (blue thin lines) is compared to the flux of the 200 cyclones that intensify least rapidly (red). Thick lines denote the arithmetic means shown in Fig. 8a. **(b)** As in **(a)** but for the lifetime-averaged flux in PW. The flux attribution percentile rank corresponds to $p = 0.9$.

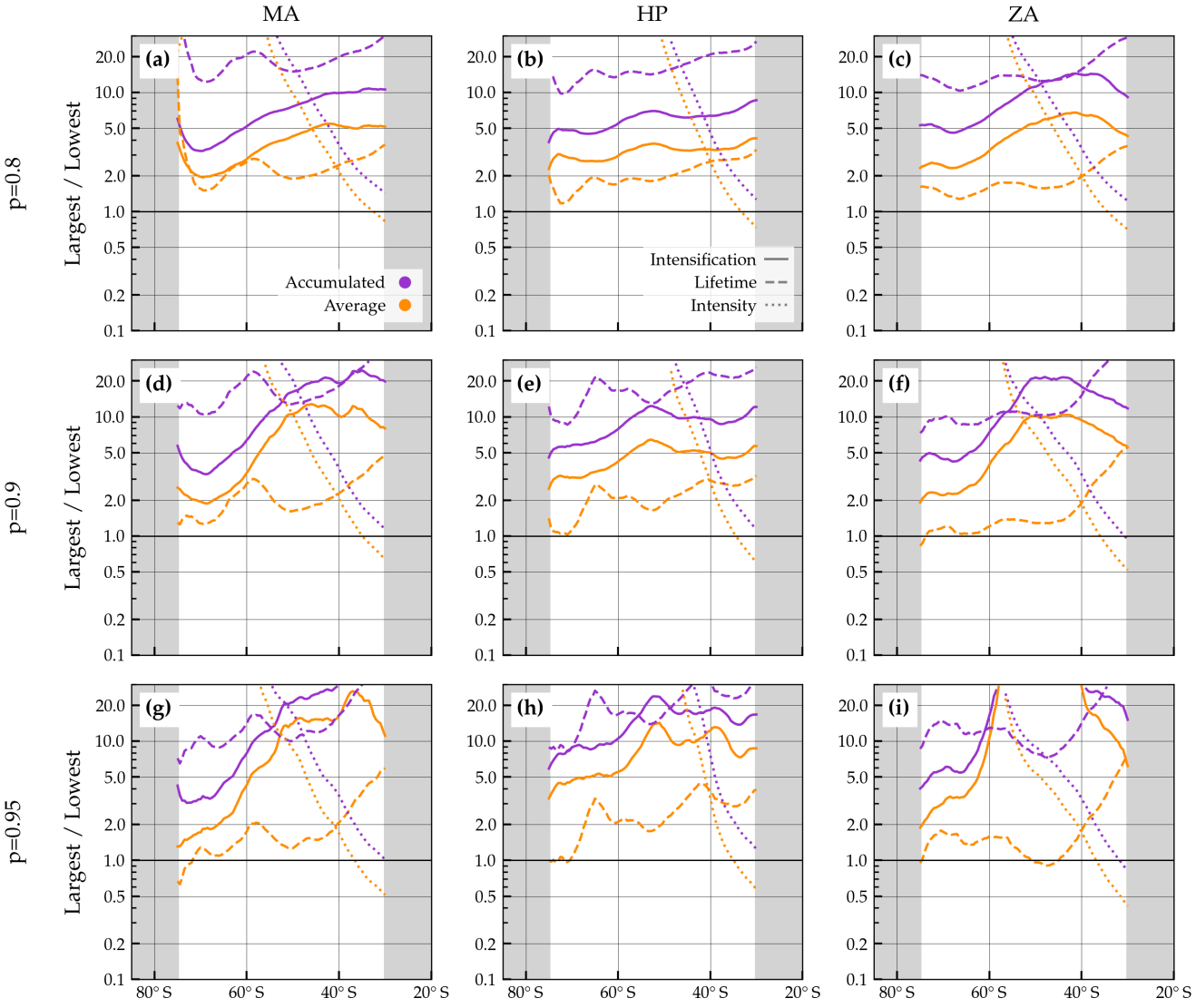

Figure D3. Ratio of the flux related to the 200 cyclones of largest vs. lowest characteristic based on all SH cyclones: Fig. 8b,d are combined and repeated for different flux decomposition methods (columns, see Sect. 2.3) and different percentile thresholds for attributing flux to cyclones (0.8, 0.9, and 0.95, see Sect. 2.4). Purple lines correspond to lifetime-accumulated fluxes, yellow lines to lifetime-averaged fluxes, and the linestyle signifies the cyclone life cycle characteristic.

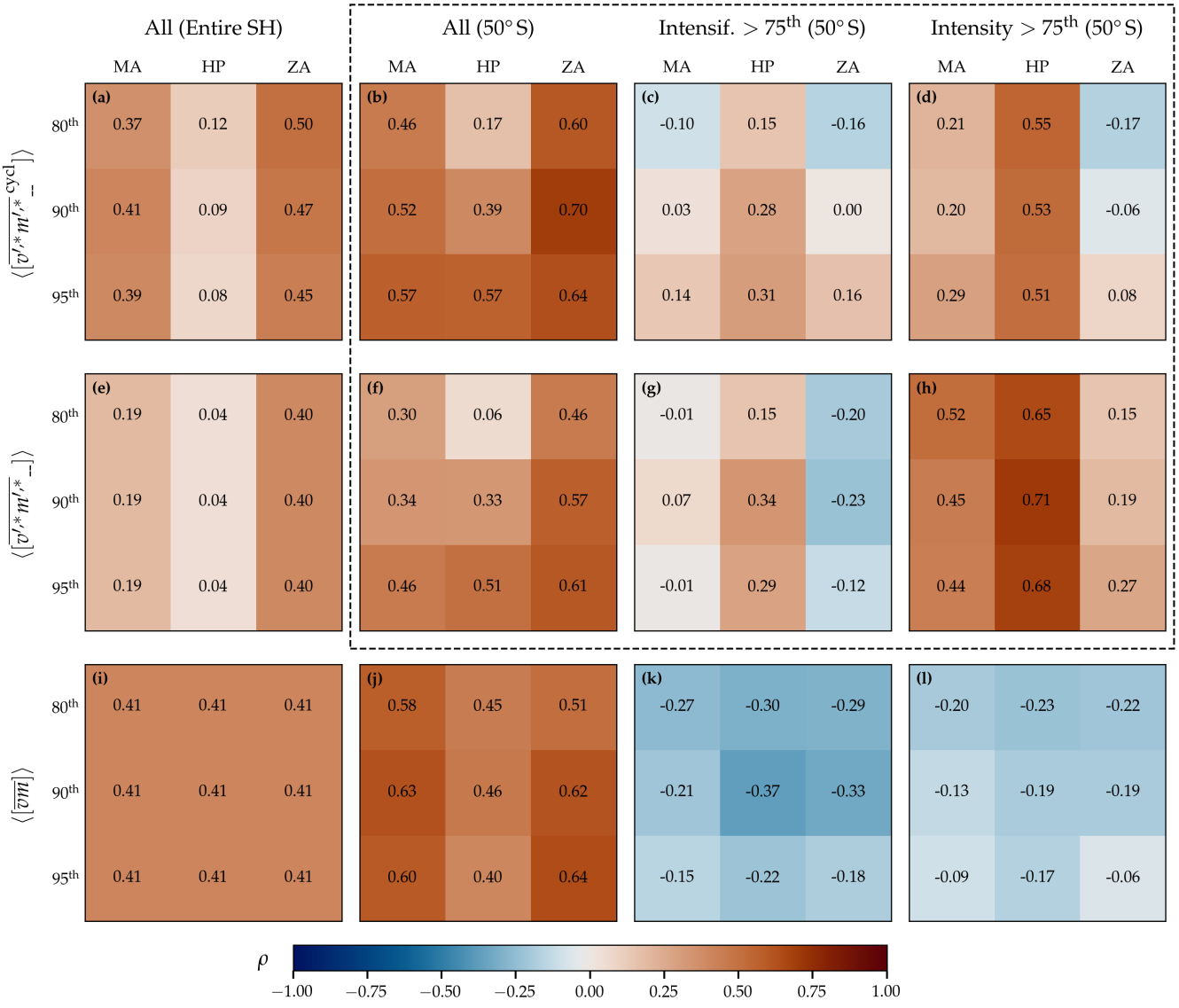

Figure E1. Sensitivity of the correlation (ρ) between seasonally averaged MSE fluxes and seasonal cyclone number to flux decomposition method and flux attribution percentile for different MSE fluxes and groups of cyclones. **(a)** The correlation of the number of all SH cyclones with cyclone-attributed eddy MSE flux, $\langle[\overline{v'^{,*}m'^{,*}}^{\text{cycl}}_{--}]\rangle$, at 50° S is shown for each percentile and flux decomposition method. Depending on the decomposition method, these fluxes correspond to temporal anomalies ($'$ for MA and HP) or zonal anomalies (* for ZA). Numerical values are accentuated with colors. Data correspond to SH JJA. This is repeated for **(b)** all cyclones with $\langle[\overline{v'^{,*}m'^{,*}}^{\text{cycl}}_{--}]\rangle \neq 0$ at 50° S, **(c)** the cyclones with $\langle[\overline{v'^{,*}m'^{,*}}^{\text{cycl}}_{--}]\rangle \neq 0$ at 50° S that have an intensification rate above the 75th climatological percentile, and **(d)** as **(c)** but for intensity instead of intensification rate. **(e–h)** as **(a–d)** but for the overall eddy MSE flux $\langle[\overline{v'^{,*}m'^{,*}}_{--}]\rangle$. **(i–l)** as **(a–d)** but for the total atmospheric MSE transport $\langle[\overline{vm}]\rangle$. The arrangement of the panels outlined by the black dashed line corresponds to the arrangement of the panels in Fig. 10.

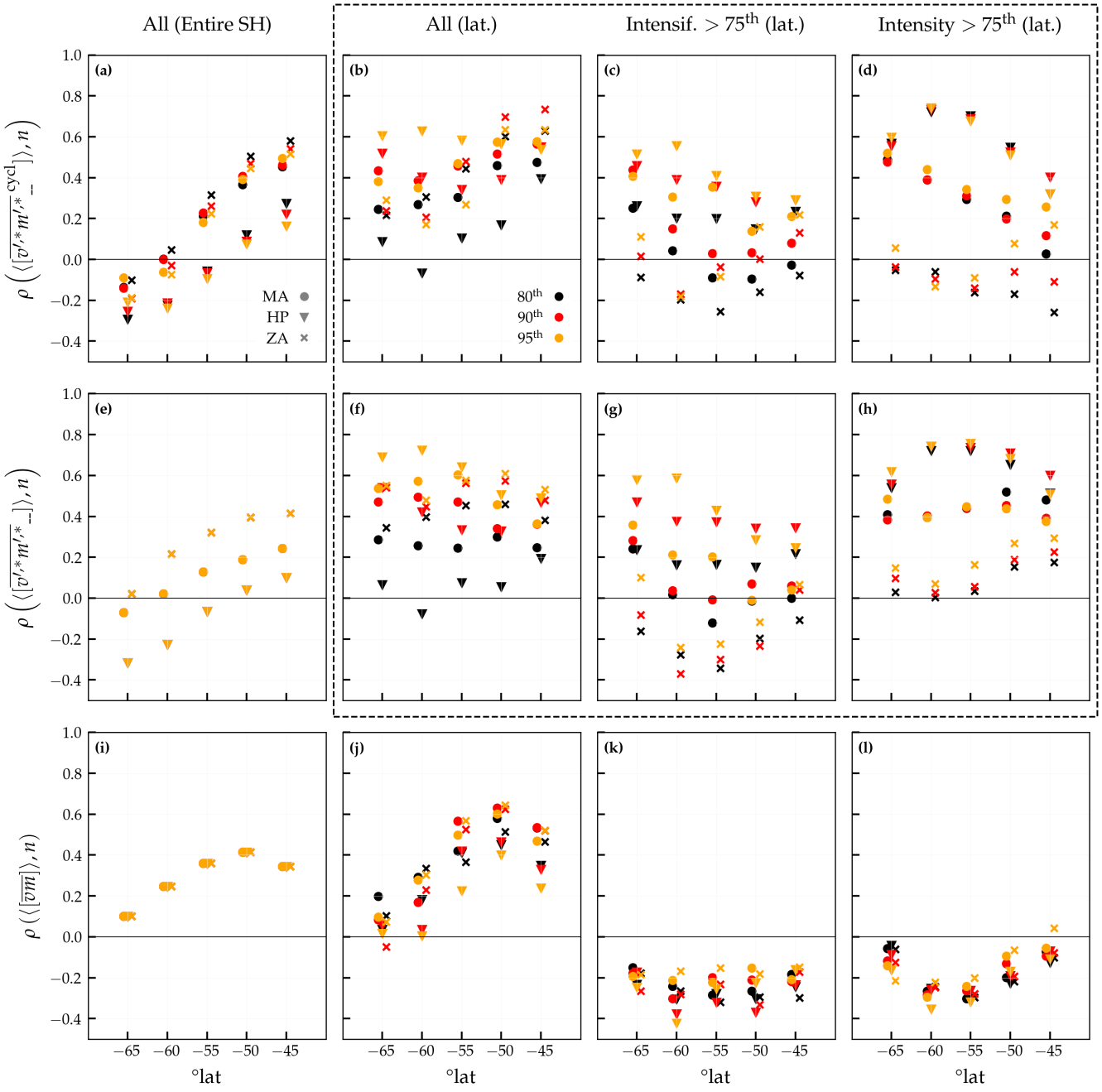

Figure E2. Sensitivity of the correlation (ρ) between seasonally averaged MSE fluxes and seasonal cyclone number to flux decomposition method and flux attribution percentile as in Fig. E1 for different latitudes. **(a)** As in Fig. E1a, the correlation of the number of all SH cyclones with cyclone-attributed eddy MSE flux, $\langle[\overline{v'^{,*}m'^{,*}}^{\mathrm{cycl}}_{--}]\rangle$, is shown here in steps of 5° latitude. Colors of the markers indicate the percentile and shapes the decomposition method. Markers for the different flux decomposition methods are slightly offset on the x-axis for better clarity. **(b–l)** as in **(a)** but for the different fluxes and groups of cyclones, arranged as in Fig. E1. The arrangement of the panels outlined by the black dashed line is consistent with Fig. 10.

Author contributions. SS conceived the project and acquired the funding. All authors contributed to the conceptualization of the study. JZ developed and implemented the methods, performed the data analysis, visualized the results, and prepared the original draft. AH supported assembling and maintaining ERA5 data. AH, AD, and SS contributed to the interpretation and discussion of the results and reviewed and edited the manuscript.

Competing interests. At least one of the (co-)authors is a member of the editorial board of Weather and Climate Dynamics. The peer-review process was guided by an independent editor, and the authors have no other competing interests to declare.

Acknowledgements. We would like to acknowledge the Applied Physics Laboratory at the University of Washington for supporting a visit which greatly fostered scientific discussions regarding the results and outline of this work. We thank colleagues at the Institute for Atmospheric and Climate Science at ETH Zurich for constructive feedback. Furthermore, we would like to thank Heini Wernli for helpful discussions and feedback on the manuscript. Moreover, we would like to thank three anonymous reviewers for their detailed feedback and helpful suggestions, which enabled us to improve the quality of this paper. The `cdo` library was used for data processing (Schulzweida, 2018). An AI-powered search engine was used for parts of code development (phind.com). J.Z., A.H., and S.S. were supported by the Swiss National Science Foundation through project grant Nr. 204181. A.D. was supported by the National Science Foundation Award AGS-2311154.

References

Armour, K. C., Siler, N., Donohoe, A., and Roe, G. H.: Meridional Atmospheric Heat Transport Constrained by Energetics and Mediated by Large-Scale Diffusion, J. Climate, 32, 3655–3680, https://doi.org/10.1175/JCLI-D-18-0563.1, 2019.

Attinger, R., Spreitzer, E., Boettcher, M., Forbes, R., Wernli, H., and Joos, H.: Quantifying the role of individual diabatic processes for the formation of PV anomalies in a North Pacific cyclone, Quarterly Journal of the Royal Meteorological Society, 145, 2454–2476, https://doi.org/10.1002/QJ.3573, 2019.

Barpanda, P. and Shaw, T.: Using the Moist Static Energy Budget to Understand Storm-Track Shifts across a Range of Time Scales, J. Atmos. Sci., 74, 2427–2446, https://doi.org/10.1175/JAS-D-17-0022.1, 2017.

Boer, G.: Some dynamical consequences of Greenhouse gas warming, Atmosphere-Ocean, 33, 731–751, https://doi.org/10.1080/07055900.1995.9649551, 1995.

Boer, G. J. and Sargent, N. E.: Vertically Integrated Budgets of Mass and Energy for the Globe, J. Atmos. Sci., 42, 1592–1613, https://doi.org/10.1175/1520-0469(1985)042<1592:VIBOMA>2.0.CO;2, 1985.

Booth, J. F., Wang, S., and Polvani, L.: Midlatitude storms in a moister world: lessons from idealized baroclinic life cycle experiments, Clim. Dynam., 41, 787–802, https://doi.org/10.1007/s00382-012-1472-3, 2013.

Büeler, D. and Pfahl, S.: Potential Vorticity Diagnostics to Quantify Effects of Latent Heating in Extratropical Cyclones. Part I: Methodology, J. Atmos. Sci., 74, 3567–3590, https://doi.org/10.1175/JAS-D-17-0041.1, 2017.

Cardinale, C. J., Rose, B. E. J., Lang, A. L., and Donohoe, A.: Stratospheric and Tropospheric Flux Contributions to the Polar Cap Energy Budgets, J. Climate, 34, 4261–4278, https://doi.org/10.1175/JCLI-D-20-0722.1, 2021.

Catto, J. L., Shaffrey, L. C., and Hodges, K. I.: Can Climate Models Capture the Structure of Extratropical Cyclones?, J. Climate, 23, 1621–1635, https://doi.org/10.1175/2009JCLI3318.1, 2010.

Chang, E. K.: Projected Significant Increase in the Number of Extreme Extratropical Cyclones in the Southern Hemisphere, J. Climate, 30, 4915–4935, https://doi.org/10.1175/JCLI-D-16-0553.1, 2017.

Chang, E. K., Guo, Y., and Xia, X.: CMIP5 multimodel ensemble projection of storm track change under global warming, J. Geophys. Res.-Atmos., 117, 23 118, https://doi.org/10.1029/2012JD018578, 2012.

Chang, E. K. M.: CMIP5 Projected Change in Northern Hemisphere Winter Cyclones with Associated Extreme Winds, J. Climate, 31, 6527–6542, https://doi.org/10.1175/JCLI-D-17-0899.1, 2018.

Clark, J. P., Feldstein, S. B., and Lee, S.: Moist Static Energy Transport Trends in Four Global Reanalyses: Are They Downgradient?, Geophys. Res. Lett., 49, https://doi.org/10.1029/2022GL098822, 2022.

Cornér, J., Bouvier, C., Doiteau, B., Pantillon, F., and Sinclair, V. A.: Classification of North Atlantic and European extratropical cyclones using multiple measures of intensity, Natural Hazards and Earth System Sciences, 25, 207–229, https://doi.org/10.5194/NHESS-25-207-2025, 2025.

Cox, T., Donohoe, A., Armour, K. C., Frierson, D. M., and Roe, G. H.: Comment on "Moist Static Energy Transport Trends in Four Global Reanalyses: Are They Downgradient?" by Clark et al. (2022), Geophysical Research Letters, 50, https://doi.org/10.1029/2023GL102804, 2023.

Cox, T., Donohoe, A., Armour, K. C., Frierson, D. M., and Roe, G. H.: Trends in Atmospheric Heat Transport Since 1980, J. Climate, 37, 1539–1550, https://doi.org/10.1175/JCLI-D-23-0385.1, 2024a.

Cox, T., Donohoe, A., Armour, K. C., Roe, G. H., and Frierson, D. M. W.: A New Method for Calculating Instantaneous Atmospheric Heat Transport, J. Climate, 37, 4337–4346, https://doi.org/10.1175/JCLI-D-23-0521.1, 2024b.

Dai, P. and Nie, J.: Robust Expansion of Extreme Midlatitude Storms Under Global Warming, Geophysical Research Letters, 49, e2022GL099 007, https://doi.org/10.1029/2022GL099007, 2022.

Donohoe, A., Armour, K. C., Roe, G. H., Battisti, D. S., and Hahn, L.: The Partitioning of Meridional Heat Transport from the Last Glacial Maximum to CO2 Quadrupling in Coupled Climate Models, J. Climate, 33, 4141–4165, https://doi.org/10.1175/JCLI-D-19-0797.1, 2020.

Eady, E. T.: Long Waves and Cyclone Waves, Tellus, 1, 33–52, https://doi.org/10.3402/tellusa.v1i3.8507, 1949.

Fearon, M. G., Doyle, J. D., Ryglicki, D. R., Finocchio, P. M., and Sprenger, M.: The Role of Cyclones in Moisture Transport into the Arctic, Geophys. Res. Lett., 48, e2020GL090 353, https://doi.org/10.1029/2020GL090353, 2021.

Franzke, C. L. E. and Harnik, N.: Long-Term Trends of the Atmospheric Circulation and Moist Static Energy Budget in the JRA-55 Reanalysis, J. Climate, pp. 1–49, https://doi.org/10.1175/jcli-d-21-0724.1, 2023.

Fritsch, F. N. and Carlson, R. E.: Monotone Piecewise Cubic Interpolation, SIAM J. Numer. Anal., 17, 238–246, https://doi.org/10.1137/0717021, 1980.

Geen, R., Czaja, A., and Haigh, J. D.: The effects of increasing humidity on heat transport by extratropical waves, Geophys. Res. Lett., 43, 8314–8321, https://doi.org/10.1002/2016GL070214, 2016.

Geng, Q. and Sugi, M.: Possible Change of Extratropical Cyclone Activity due to Enhanced Greenhouse Gases and Sulfate Aerosols—Study with a High-Resolution AGCM, J. Climate, 16, 2262–2274, https://doi.org/10.1175/1520-0442(2003)16<2262:PCOECA>2.0.CO;2, 2003.

Grieger, J., Leckebusch, G. C., Donat, M. G., Schuster, M., and Ulbrich, U.: Southern Hemisphere winter cyclone activity under recent and future climate conditions in multi-model AOGCM simulations, Int. J. Climatol., 34, 3400–3416, https://doi.org/10.1002/JOC.3917, 2014.

Heitmann, K., Sprenger, M., Binder, H., Wernli, H., and Joos, H.: Warm conveyor belt characteristics and impacts along the life cycle of extratropical cyclones: case studies and climatological analysis based on ERA5, Weather Clim. Dynam., 5, 537–557, https://doi.org/10.5194/wcd-5-537-2024, 2024.

Hersbach, H., Bell, B., Berrisford, P., Hirahara, S., Horányi, A., Muñoz-Sabater, J., Nicolas, J., Peubey, C., Radu, R., Schepers, D., Simmons, A., Soci, C., Abdalla, S., Abellan, X., Balsamo, G., Bechtold, P., Biavati, G., Bidlot, J., Bonavita, M., Chiara, G., Dahlgren, P., Dee, D., Diamantakis, M., Dragani, R., Flemming, J., Forbes, R., Fuentes, M., Geer, A., Haimberger, L., Healy, S., Hogan, R. J., Hólm, E., Janisková, M., Keeley, S., Laloyaux, P., Lopez, P., Lupu, C., Radnoti, G., Rosnay, P., Rozum, I., Vamborg, F., Villaume, S., and Thépaut, J.: The ERA5 global reanalysis, Q.J. Roy. Meteor. Soc., 146, 1999–2049, https://doi.org/10.1002/qj.3803, 2020.

Hoskins, B. J., James, I. N., and White, G. H.: The Shape, Propagation and Mean-Flow Interaction of Large-Scale Weather Systems, J. Atmos. Sci., 40, 1595–1612, https://doi.org/10.1175/1520-0469(1983)040<1595:TSPAMF>2.0.CO;2, 1983.

Kang, J. M., Shaw, T. A., Kang, S. M., Simpson, I. R., and Yu, Y.: Revisiting the reanalysis-model discrepancy in Southern Hemisphere winter storm track trends, npj Clim. Atmos. Sci., 7, 1–10, https://doi.org/10.1038/s41612-024-00801-3, 2024.

Kaspi, Y. and Schneider, T.: The Role of Stationary Eddies in Shaping Midlatitude Storm Tracks, J. Atmos. Sci., 70, 2596–2613, https://doi.org/10.1175/JAS-D-12-082.1, 2013.

Kolstad, E. W. and Bracegirdle, T. J.: Marine cold-air outbreaks in the future: An assessment of IPCC AR4 model results for the Northern Hemisphere, Clim. Dynam., 30, 871–885, https://doi.org/10.1007/S00382-007-0331-0/FIGURES/10, 2008.

König, W., Sausen, R., and Sielmann, F.: Objective Identification of Cyclones in GCM Simulations, J. Climate, 6, 2217–2231, https://doi.org/10.1175/1520-0442(1993)006<2217:OIOCIG>2.0.CO;2, 1993.

Lambert, S. J. and Fyfe, J. C.: Changes in winter cyclone frequencies and strengths simulated in enhanced greenhouse warming experiments: Results from the models participating in the IPCC diagnostic exercise, Climate Dynamics, 26, 713–728, https://doi.org/10.1007/S00382-006-0110-3/TABLES/4, 2006.

Lembo, V., Fabiano, F., Galfi, V. M., Graversen, R. G., Lucarini, V., and Messori, G.: Meridional-energy-transport extremes and the general circulation of Northern Hemisphere mid-latitudes: dominant weather regimes and preferred zonal wavenumbers, Weather Clim. Dynam., 3, 1037–1062, https://doi.org/10.5194/wcd-3-1037-2022, 2022.

Lindzen, R. S. and Farrell, B.: A Simple Approximate Result for the Maximum Growth Rate of Baroclinic Instabilities, Journal of the Atmospheric Sciences, 37, 1648–1654, https://doi.org/10.1175/1520-0469(1980)037<1648:ASARFT>2.0.CO;2, 1980.

Lopez-Marti, F., Ginesta, M., Faranda, D., Rutgersson, A., Yiou, P., Wu, L., and Messori, G.: Future changes in compound explosive cyclones and atmospheric rivers in the North Atlantic, Earth Sys. Dynam., 16, 169–187, https://doi.org/10.5194/ESD-16-169-2025, 2025.

Marshall, J., Donohoe, A., Ferreira, D., and McGee, D.: The ocean's role in setting the mean position of the Inter-Tropical Convergence Zone, Clim. Dynam., 42, 1967–1979, https://doi.org/10.1007/s00382-013-1767-z, 2014.

Mayer, J., Mayer, M., and Haimberger, L.: Consistency and Homogeneity of Atmospheric Energy, Moisture, and Mass Budgets in ERA5, Journal of Climate, 34, 3955–3974, https://doi.org/10.1175/JCLI-D-20-0676.1, 2021.

Mayer, M., Kato, S., Bosilovich, M., Bechtold, P., Mayer, J., Schröder, M., Behrangi, A., Wild, M., Kobayashi, S., Li, Z., and L'Ecuyer, T.: Assessment of Atmospheric and Surface Energy Budgets Using Observation-Based Data Products, Surv. Geophys., pp. 1–28, https://doi.org/10.1007/S10712-024-09827-X/TABLES/5, 2024.

Messori, G. and Czaja, A.: On the sporadic nature of meridional heat transport by transient eddies, Q.J. Roy. Meteor. Soc., 139, 999–1008, https://doi.org/10.1002/qj.2011, 2013.

Messori, G. and Czaja, A.: Some considerations on the spectral features of meridional heat transport by transient eddies, Q.J. Roy. Meteor. Soc., 140, 1377–1386, https://doi.org/10.1002/QJ.2224, 2014.

Messori, G. and Czaja, A.: On local and zonal pulses of atmospheric heat transport in reanalysis data, Q.J. Roy. Meteor. Soc., 141, 2376–2389, https://doi.org/10.1002/qj.2529, 2015.

Messori, G., Geen, R., and Czaja, A.: On the spatial and temporal variability of atmospheric heat transport in a hierarchy of models, J. Atmos. Sci., 74, 2163–2189, https://doi.org/10.1175/JAS-D-16-0360.1, 2017.

Neelin, J. D. and Held, I. M.: Modeling Tropical Convergence Based on the Moist Static Energy Budget, Mon. Weather Rev., 115, 3–12, https://doi.org/10.1175/1520-0493(1987)115<0003:MTCBOT>2.0.CO;2, 1987.

Novak, L., Ambaum, M. H. P., and Tailleux, R.: The Life Cycle of the North Atlantic Storm Track, J. Atmos. Sci., 72, 821–833, https://doi.org/10.1175/JAS-D-14-0082.1, 2015.

Papritz, L., Pfahl, S., Rudeva, I., Simmonds, I., Sodemann, H., and Wernli, H.: The Role of Extratropical Cyclones and Fronts for Southern Ocean Freshwater Fluxes, J. Climate, 27, 6205–6224, https://doi.org/10.1175/JCLI-D-13-00409.1, 2014.

Peixoto, J. P. and Oort, A. H.: Physics of climate, American Institute of Physics, Melville, New York, 1992.

Priestley, C. H.: Heat transport and zonal stress between latitudes, Q.J. Roy. Meteor. Soc., 75, 28–40, https://doi.org/10.1002/qj.49707532307, 1949.

Priestley, M. D. K. and Catto, J. L.: Future changes in the extratropical storm tracks and cyclone intensity, wind speed, and structure, Weather Clim. Dynam., 3, 337–360, https://doi.org/10.5194/wcd-3-337-2022, 2022.

Rudeva, I. and Gulev, S. K.: Climatology of Cyclone Size Characteristics and Their Changes during the Cyclone Life Cycle, Mon. Weather Rev., 135, 2568–2587, https://doi.org/10.1175/MWR3420.1, 2007.

Rudeva, I., Simmonds, I., Crock, D., and Boschat, G.: Midlatitude Fronts and Variability in the Southern Hemisphere Tropical Width, Journal of Climate, 32, 8243–8260, https://doi.org/10.1175/JCLI-D-18-0782.1, 2019.

Rüdisühli, S., Sprenger, M., Leutwyler, D., Schär, C., and Wernli, H.: Attribution of precipitation to cyclones and fronts over Europe in a kilometer-scale regional climate simulation, Weather and Climate Dynamics, 1, 675–699, https://doi.org/10.5194/wcd-1-675-2020, 2020.

Ruggieri, P., Alvarez-Castro, M. C., Athanasiadis, P., Bellucci, A., Materia, S., and Gualdi, S.: North Atlantic Circulation Regimes and Heat Transport by Synoptic Eddies, J. Climate, 33, 4769–4785, https://doi.org/10.1175/JCLI-D-19-0498.1, 2020.

Rydsaa, J. H., Graversen, R. G., Heiskanen, T. I., and Stoll, P. J.: Changes in atmospheric latent energy transport into the Arctic: Planetary versus synoptic scales, Q.J. Roy. Meteor. Soc., 147, 2281–2292, https://doi.org/10.1002/QJ.4022, 2021.

Sanders, F. and Gyakum, J. R.: Synoptic-Dynamic Climatology of the "Bomb", Mon. Weather Rev., 108, 1589–1606, https://doi.org/10.1175/1520-0493(1980)108<1589:SDCOT>2.0.CO;2, 1980.

Schemm, S. and Rivière, G.: On the Efficiency of Baroclinic Eddy Growth and How It Reduces the North Pacific Storm-Track Intensity in Midwinter, J. Climate, 32, 8373–8398, https://doi.org/10.1175/JCLI-D-19-0115.1, 2019.

Schemm, S. and Sprenger, M.: Frontal-wave cyclogenesis in the North Atlantic –a climatological characterisation, Quarterly Journal of the Royal Meteorological Society, 141, 2989–3005, https://doi.org/10.1002/qj.2584, 2015.

Schemm, S., Rudeva, I., and Simmonds, I.: Extratropical fronts in the lower troposphere–global perspectives obtained from two automated methods, Quarterly Journal of the Royal Meteorological Society, 141, 1686–1698, https://doi.org/10.1002/QJ.2471, 2015.

Schemm, S., Sprenger, M., and Wernli, H.: When during Their Life Cycle Are Extratropical Cyclones Attended by Fronts?, B. Am. Meteorol. Soc., 99, 149–165, https://doi.org/10.1175/BAMS-D-16-0261.1, 2018.

Schemm, S., Papritz, L., and Rivière, G.: Storm track response to uniform global warming downstream of an idealized sea surface temperature front, Weather Clim. Dynam., 3, 601–623, https://doi.org/10.5194/wcd-3-601-2022, 2022.

Schulzweida, U.: CDO User Guide, https://doi.org/10.5281/ZENODO.1435455, 2018.

Seiler, C. and Zwiers, F. W.: How will climate change affect explosive cyclones in the extratropics of the Northern Hemisphere?, Clim. Dynam., 46, 3633–3644, https://doi.org/10.1007/S00382-015-2791-Y/FIGURES/6, 2016.

Shapiro, M. A. and Keyser, D.: Fronts, Jet Streams and the Tropopause, in: Extratropical Cyclones: The Erik Palmén Memorial Volume, edited by W., N. C. and Holopainen, E. O., pp. 167–191, American Meteorological Society, Boston, MA, ISBN 978-1-944970-33-8, https://doi.org/10.1007/978-1-944970-33-8_10, 1990.

Shaw, T. A., Baldwin, M., Barnes, E. A., Caballero, R., Garfinkel, C. I., Hwang, Y. T., Li, C., O'Gorman, P. A., Rivière, G., Simpson, I. R., and Voigt, A.: Storm track processes and the opposing influences of climate change, Nature Geoscience, 9, 656–664, https://doi.org/10.1038/ngeo2783, 2016.

Shaw, T. A., Barpanda, P., and Donohoe, A.: A Moist Static Energy Framework for Zonal-Mean Storm-Track Intensity, J. Atmos. Sci., 75, 1979–1994, https://doi.org/10.1175/JAS-D-17-0183.1, 2018.

Shields, C. A., Rutz, J. J., Leung, L. Y., Martin Ralph, F., Wehner, M., Kawzenuk, B., Lora, J. M., McClenny, E., Osborne, T., Payne, A. E., Ullrich, P., Gershunov, A., Goldenson, N., Guan, B., Qian, Y., Ramos, A. M., Sarangi, C., Sellars, S., Gorodetskaya, I., Kashinath, K., Kurlin, V., Mahoney, K., Muszynski, G., Pierce, R., Subramanian, A. C., Tome, R., Waliser, D., Walton, D., Wick, G., Wilson, A., Lavers, D., Prabhat, Collow, A., Krishnan, H., Magnusdottir, G., and Nguyen, P.: Atmospheric River Tracking Method Intercomparison Project (ARTMIP): Project goals and experimental design, Geosci. Model Dev., 11, 2455–2474, https://doi.org/10.5194/GMD-11-2455-2018, 2018.

Simmons, A. J.: Trends in the tropospheric general circulation from 1979 to 2022, Weather Clim. Dynam., 3, 777–809, https://doi.org/10.5194/wcd-3-777-2022, 2022.

Sinclair, V. A. and Catto, J. L.: The relationship between extra-tropical cyclone intensity and precipitation in idealised current and future climates, Weather and Climate Dynamics Discussions, https://doi.org/doi.org/10.5194/wcd-2022-62, 2022.

Sinclair, V. A. and Dacre, H. F.: Which Extratropical Cyclones Contribute Most to the Transport of Moisture in the Southern Hemisphere?, J. Geophys. Res.-Atmos., 124, 2525–2545, https://doi.org/10.1029/2018JD028766, 2019.

Sinclair, V. A., Rantanen, M., Haapanala, P., Räisänen, J., and Järvinen, H.: The characteristics and structure of extra-tropical cyclones in a warmer climate, Weather Clim. Dynam., 1, 1–25, https://doi.org/10.5194/wcd-1-1-2020, 2020.

Sprenger, M., Fragkoulidis, G., Binder, H., Croci-Maspoli, M., Graf, P., Grams, C. M., Knippertz, P., Madonna, E., Schemm, S., Škerlak, B., and Wernli, H.: Global Climatologies of Eulerian and Lagrangian Flow Features based on ERA-Interim, B. Am. Meteorol. Soc., 98, 1739–1748, https://doi.org/10.1175/BAMS-D-15-00299.1, 2017.

Stoll, P. J., Graversen, R. G., and Messori, G.: The global atmospheric energy transport analysed by a wavelength-based scale separation, Weather Clim. Dynam., 4, 1–17, https://doi.org/10.5194/WCD-4-1-2023, 2023.

Thorncroft, C. D., Hoskins, B. J., and McIntyre, M. E.: Two paradigms of baroclinic-wave life-cycle behaviour, Quarterly Journal of the Royal Meteorological Society, 119, 17–55, https://doi.org/10.1002/qj.49711950903, 1993.

Trenberth, K. E.: Climate Diagnostics from Global Analyses: Conservation of Mass in ECMWF Analyses, Journal of Climate, 4, 707–722, https://doi.org/10.1175/1520-0442(1991)004<0707:CDFGAC>2.0.CO;2, 1991.

Tsukernik, M. and Lynch, A. H.: Atmospheric Meridional Moisture Flux over the Southern Ocean: A Story of the Amundsen Sea, J. Climate, 26, 8055–8064, https://doi.org/10.1175/JCLI-D-12-00381.1, 2013.

Ullrich, P. A., Zarzycki, C. M., McClenny, E. E., Pinheiro, M. C., Stansfield, A. M., and Reed, K. A.: TempestExtremes v2.1: A community framework for feature detection, tracking, and analysis in large datasets, Geosci. Model Dev., 14, 5023–5048, https://doi.org/10.5194/GMD-14-5023-2021, 2021.

Vannière, B., Czaja, A., Dacre, H., Woollings, T., and Parfitt, R.: A potential vorticity signature for the cold sector of winter extratropical cyclones, Q.J. Roy. Meteor. Soc., 142, 432–442, https://doi.org/10.1002/QJ.2662, 2016.

Wernli, H. and Schwierz, C.: Surface Cyclones in the ERA-40 Dataset (1958–2001). Part I: Novel Identification Method and Global Climatology, J. Atmos. Sci., 63, https://doi.org/10.1175/JAS3766.1, 2006.

Zhang, Y. and Wang, W.-C.: Model-Simulated Northern Winter Cyclone and Anticyclone Activity under a Greenhouse Warming Scenario, J. Climate, 10, 1616–1634, https://doi.org/10.1175/1520-0442(1997)010<1616:MSNWCA>2.0.CO;2, 1997.

Zolina, O. and Gulev, S. K.: Synoptic Variability of Ocean–Atmosphere Turbulent Fluxes Associated with Atmospheric Cyclones, J. Climate, 16, 2717–2734, https://doi.org/10.1175/1520-0442(2003)016<2717:SVOOTF>2.0.CO;2, 2003.